Medical Physics
The International Journal of Medical Physics Research and Practice

# Oblique reconstructions in tomosynthesis. II. Super-resolution

Raymond J. Acciavatti and Andrew D. A. Maidment

Citation: Medical Physics **40**, 111912 (2013); doi: 10.1118/1.4819942
View online: http://dx.doi.org/10.1118/1.4819942
View Table of Contents: http://scitation.aip.org/content/aapm/journal/medphys/40/11?ver=pdfcov
Published by the American Association of Physicists in Medicine

# Oblique reconstructions in tomosynthesis. II. Super-resolution

Raymond J. Acciavatti and Andrew D. A. Maidment[a)]
*Department of Radiology, Perelman School of Medicine at the University of Pennsylvania, Philadelphia, Pennsylvania 19104-4206*

(Received 18 May 2013; revised 4 August 2013; accepted for publication 12 August 2013; published 11 October 2013)

**Purpose:** In tomosynthesis, super-resolution has been demonstrated using reconstruction planes parallel to the detector. Super-resolution allows for subpixel resolution relative to the detector. The purpose of this work is to develop an analytical model that generalizes super-resolution to oblique reconstruction planes.
**Methods:** In a digital tomosynthesis system, a sinusoidal test object is modeled along oblique angles (i.e., "pitches") relative to the plane of the detector in a 3D divergent-beam acquisition geometry. To investigate the potential for super-resolution, the input frequency is specified to be greater than the alias frequency of the detector. Reconstructions are evaluated in an oblique plane along the extent of the object using simple backprojection (SBP) and filtered backprojection (FBP). By comparing the amplitude of the reconstruction against the attenuation coefficient of the object at various frequencies, the modulation transfer function (MTF) is calculated to determine whether modulation is within detectable limits for super-resolution. For experimental validation of super-resolution, a goniometry stand was used to orient a bar pattern phantom along various pitches relative to the breast support in a commercial digital breast tomosynthesis system.
**Results:** Using theoretical modeling, it is shown that a single projection image cannot resolve a sine input whose frequency exceeds the detector alias frequency. The high frequency input is correctly visualized in SBP or FBP reconstruction using a slice along the pitch of the object. The Fourier transform of this reconstructed slice is maximized at the input frequency as proof that the object is resolved. Consistent with the theoretical results, experimental images of a bar pattern phantom showed super-resolution in oblique reconstructions. At various pitches, the highest frequency with detectable modulation was determined by visual inspection of the bar patterns. The dependency of the highest detectable frequency on pitch followed the same trend as the analytical model. It was demonstrated that super-resolution is not achievable if the pitch of the object approaches 90°, corresponding to the case in which the test frequency is perpendicular to the breast support. Only low frequency objects are detectable at pitches close to 90°.
**Conclusions:** This work provides a platform for investigating super-resolution in oblique reconstructions for tomosynthesis. In breast imaging, this study should have applications in visualizing microcalcifications and other subtle signs of cancer.  [http://dx.doi.org/10.1118/1.4819942]

Key words: tomosynthesis, super-resolution, oblique reconstruction, modulation transfer function (MTF), bar pattern phantom

## 1. INTRODUCTION

In tomosynthesis, a volumetric reconstruction is generated from projection images acquired over a small angular range. Our previous studies proposed a conceptual test object known as a sine plate for assessing image quality in tomosynthesis.[1–7] This object is a thin strip whose attenuation coefficient varies sinusoidally. Increasing the frequency of the object simulates small closely-spaced structures such as microcalcifications, which are early indicators of cancer in breast imaging applications.[8] The sine plate has led to the discovery of super-resolution in tomosynthesis.[1,5] Super-resolution is a term which describes the ability to resolve input frequencies higher than the detector alias frequency, or the frequency above which high frequency information is represented as if it were low frequency information in a single projection.[5]

Super-resolution arises because the image of an object is translated in subpixel detector element increments between projections. To observe super-resolution, it is necessary to perform the reconstruction with a matrix whose pixel size is much smaller than that of the detector elements. The existence of super-resolution was verified experimentally with a bar pattern phantom[1,5] using a commercial digital breast tomosynthesis (DBT) x-ray unit and a commercial prototype reconstruction solution[9] (Briona$^{TM}$, Real Time Tomography, Villanova, PA). In DBT, super-resolution has applications in improving the visibility of microcalcifications and other subtle signs of breast cancer.

By orienting the long axis of the sine plate along various "pitch" angles relative to the plane of the detector, we have also demonstrated the feasibility of oblique reconstructions in tomosynthesis.[7] To analyze image quality at various test frequencies, the modulation transfer function (MTF) was calculated from the relative amplitude of the reconstruction. This approach addressed some of the simplifying assumptions made in Zhao's model of MTF for tomosynthesis.[10] Although Zhao's model assumes the use of reconstructed slices parallel to the detector, the sine plate provided a framework for determining the MTF in oblique slices. In addition, the sine plate was used to model the effect of object thickness on the MTF.

Our previous work on oblique reconstructions does not model detector pixelation, and thus does not explicitly show that test frequencies exceeding the detector alias frequency can be reconstructed at various pitches. This study extends our analysis of super-resolution to oblique reconstruction planes. To determine whether the thickness of the object places limits on the feasibility of super-resolution, this study also generalizes the MTF calculation to a digital system. For experimental proof of both resolution and super-resolution in oblique reconstructions, projection images of a bar pattern phantom were acquired and subsequently reconstructed.

## 2. METHODS

### 2.A. Pitched sine plate

A framework for investigating super-resolution in oblique reconstructions for tomosynthesis is now developed. Accordingly, we calculate the reconstruction of a rectangular prism whose linear attenuation coefficient varies sinusoidally along the pitch angle, $\alpha_y$. The object is modeled by a rectangular prism, since this shape allows us to analyze the effect of object thickness on in-plane resolution, similar to our previous work.[7] As shown in Fig. 1, the pitch angle corresponds to a rotation of the $x$ and $z$ axes about the $y$ axis perpendicular to the plane of x-ray tube motion (i.e., the $xz$ plane). In DBT, the breast is positioned so that the chest wall lies in the plane of x-ray tube motion, and hence, the $y$ axis is the chest wall-to-nipple direction. The matrix transformation corresponding to the pitch rotation about the $y$ axis is

$$\begin{pmatrix} \mathbf{i}'' \\ \mathbf{j}'' \\ \mathbf{k}'' \end{pmatrix} = \begin{pmatrix} \cos\alpha_y & 0 & \sin\alpha_y \\ 0 & 1 & 0 \\ -\sin\alpha_y & 0 & \cos\alpha_y \end{pmatrix} \begin{pmatrix} \mathbf{i} \\ \mathbf{j} \\ \mathbf{k} \end{pmatrix}, \tag{1}$$

where $\mathbf{i}$, $\mathbf{j}$, and $\mathbf{k}$ are orthogonal unit vectors in the $x$, $y$, and $z$ directions, respectively, and where $\mathbf{i}''$, $\mathbf{j}''$, and $\mathbf{k}''$ are the transformed unit vectors. One can introduce a vector to model the input frequency ($f_0$) along the pitch angle, $\alpha_y$. To investigate the potential for super-resolution, this frequency is taken to be higher than the alias frequency of the detector

$$\mathbf{f_0} = f_0\mathbf{i}'' \tag{2}$$

$$= f_0[(\cos\alpha_y)\mathbf{i} + (\sin\alpha_y)\mathbf{k}]. \tag{3}$$

Figure 1 shows a cross section of the input object in the plane of x-ray tube motion. The object has infinite extent in the $\mathbf{i}''$ and $\mathbf{j}''$ directions. Defining the origin (O) as the midpoint of the chest wall side of the detector, the attenuation coefficient of the object can thus be written as

$$\mu(x, y, z) = C \cdot \cos\left(2\pi \mathbf{f_0} \bullet [\mathbf{r} - \mathbf{r_0}]\right) \cdot \mathrm{rect}\left(\frac{\mathbf{k}'' \bullet [\mathbf{r} - \mathbf{r_0}]}{\varepsilon}\right), \tag{4}$$

where $\mathbf{r}$ is a position vector from O to any point $(x, y, z)$ in $\mathbb{R}^3$, $\mathbf{r_0}$ denotes a vector from O to a known point $(x_0, y_0, z_0)$ in

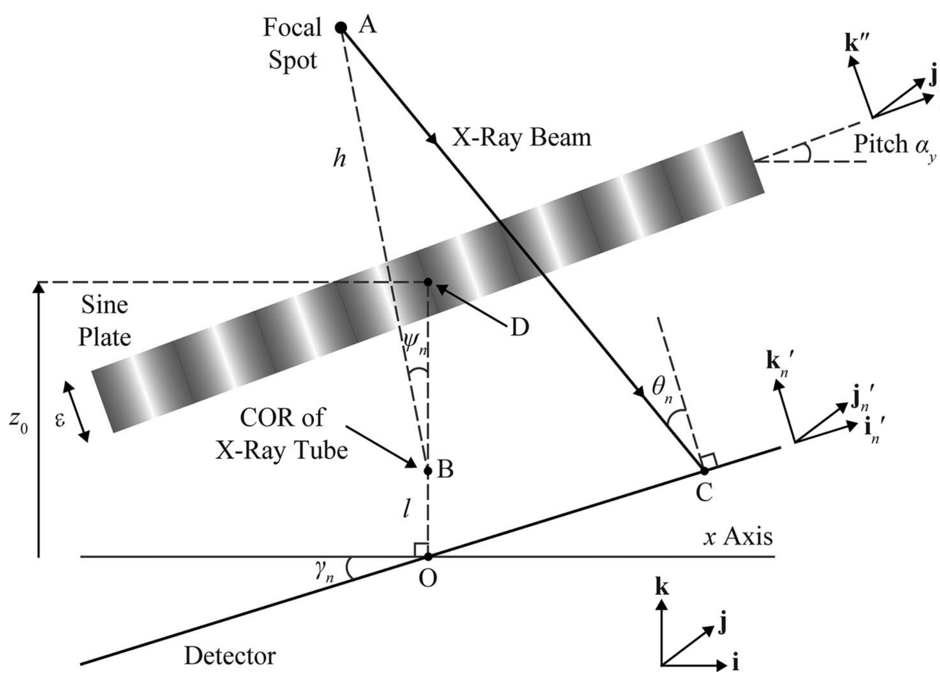


FIG. 1. A pitched sine plate is used to investigate the potential for super-resolution in oblique reconstructions for tomosynthesis. The pitch axis along the angle $\alpha_y$ relative to the $\mathbf{i}$ direction lies within the plane of x-ray tube motion (i.e., the $xz$ plane). Although a 2D cross section of the object is shown, it is assumed that the object has infinite extent in the $+y$ direction. In acquiring the $n$th projection image, the x-ray tube rotates about point B at the angle $\psi_n$ relative to the $z$ direction. The detector rotates about the $y$ axis at the angle $\gamma_n$ relative to the $x$ direction.

the object, $C$ is the maximum value of the attenuation coefficient, $\varepsilon$ indicates the object thickness along the $\mathbf{k}''$ direction, and

$$\mathrm{rect}(u) \equiv \begin{cases} 1, & |u| \le 1/2 \\ 0, & |u| > 1/2. \end{cases} \tag{5}$$

Combining Eqs. (1), (3), and (4) yields

$$\mu(x, y, z) = C \cdot \cos(2\pi f_0[(x - x_0)\cos\alpha_y + (z - z_0)\sin\alpha_y]) \cdot \mathrm{rect}\left[\frac{-(x - x_0)\sin\alpha_y + (z - z_0)\cos\alpha_y}{\varepsilon}\right] \tag{6}$$

completing the formalism of the attenuation coefficient.

### 2.B. Digital detector signal

To calculate detector signal for the $n$th projection, it is useful to perform ray tracing between the focal spot at A and the incident point on the detector at C (Fig. 1). The most general tomosynthesis geometry with a divergent x-ray beam and a rotating detector is analyzed. Following our previous work,[5] the vector from the origin to point C on the detector is written as

$$\overrightarrow{\mathrm{OC}} = u_1\mathbf{i}'_n + u_2\mathbf{j}'_n, \tag{7}$$

where $u_1$ measures detector position within the plane of the x-ray tube motion and $u_2$ measures position along the perpendicular direction. The unit vectors $\mathbf{i}'_n$ and $\mathbf{j}'_n$ are determined from detector rotation about the $y$ axis at the angle $\gamma_n$

$$\begin{pmatrix} \mathbf{i}'_n \\ \mathbf{j}'_n \\ \mathbf{k}'_n \end{pmatrix} = \begin{pmatrix} \cos\gamma_n & 0 & \sin\gamma_n \\ 0 & 1 & 0 \\ -\sin\gamma_n & 0 & \cos\gamma_n \end{pmatrix} \begin{pmatrix} \mathbf{i} \\ \mathbf{j} \\ \mathbf{k} \end{pmatrix}. \tag{8}$$

Each projection angle $\psi_n$ relative to the $z$ axis is calculated from the angular spacing between projections ($\Delta\psi$) as

$$\psi_n = n \cdot \Delta\psi, \tag{9}$$

so that

$$\gamma_n = \frac{\psi_n}{g}, \tag{10}$$

where $g$ denotes the gear ratio of the detector and where the projection number $n$ varies between $-(N-1)/2$ and $+(N-1)/2$. In our prior study, the parametric equations for the ray between the focal spot at A and the incident point on the detector at C have been determined

$$x = w(u_1\cos\gamma_n + h\sin\psi_n) - h\sin\psi_n, \tag{11}$$

$$y = wu_2, \tag{12}$$

$$z = w(u_1\sin\gamma_n - l - h\cos\psi_n) + l + h\cos\psi_n. \tag{13}$$

In these expressions, $h$ is the distance between the focal spot and the center-of-rotation (COR) of the x-ray tube, $l$ is the COR-to-origin distance (Fig. 1), and $w$ is a free parameter ranging between zero and unity. The x-ray path length $\mathcal{L}_n$ through the input object is now derived from these parametric equations by calculating the points of intersection of the x-ray beam with the planar surfaces of the sine plate. Using Eqs. (5) and (6), it can be shown that the planar surfaces of the object can be modeled by the expression

$$z_\pm = (x - x_0)\tan\alpha_y + z_0 \pm (\varepsilon/2)\sec\alpha_y, \tag{14}$$

where the "+" and "−" symbols correspond to the x-ray entrance and exit surfaces, respectively. Denoting $x_n^\pm$ and $w_n^\pm$ as the values of $x$ and $w$ at these two surfaces, it follows from Eq. (11) that

$$w_n^\pm = \frac{x_n^\pm + h\sin\psi_n}{u_1\cos\gamma_n + h\sin\psi_n} \tag{15}$$

and from Eqs. (13) and (14) that

$$w_n^\pm = \frac{(x_n^\pm - x_0)\tan\alpha_y + z_0 \pm (\varepsilon/2)\sec\alpha_y - l - h\cos\psi_n}{u_1\sin\gamma_n - l - h\cos\psi_n}. \tag{16}$$

Equations (15) and (16) provide a system of two equations in two unknowns ($x_n^\pm$ and $w_n^\pm$). Using a computer algebra system (Maple 16, Maplesoft, Waterloo, Ontario) to solve for the two unknowns, $w_n^\pm$ can be written in a form that does not depend on $x_n^\pm$

$$w_n^\pm = \frac{z_0 - l - h\cos\psi_n - (x_0 + h\sin\psi_n)\tan\alpha_y \pm (\varepsilon/2)\sec\alpha_y}{u_1\sin\gamma_n - l - h\cos\psi_n - (u_1\cos\gamma_n + h\sin\psi_n)\tan\alpha_y}. \tag{17}$$

Total x-ray attenuation $\mathcal{A}\mu(n)$ for the $n$th projection is now found by integrating $\mu(x, y, z)$ along $\mathcal{L}_n$

$$\mathcal{A}\mu(n) = \int_{\mathcal{L}_n} \mu ds. \tag{18}$$

From our previous work, the differential arc length $ds$ along $\mathcal{L}_n$ is

$$ds = \left[h\cos(\psi_n - \gamma_n) + l\cos\gamma_n\right]\sec(\theta_n) \cdot dw, \tag{19}$$

where $\theta_n$ is the angle of x-ray incidence relative to $\mathbf{k}'_n$

$$\theta_n = \arccos\left[\frac{h\cos(\psi_n-\gamma_n)+l\cos\gamma_n}{\sqrt{(u_1\cos\gamma_n+h\sin\psi_n)^2+u_2^2+(l+h\cos\psi_n-u_1\sin\gamma_n)^2}}\right]. \tag{20}$$

By combining Eqs. (6), (11), (13), (18), and (19), the total x-ray attenuation for each projection can now be calculated in closed form

$$\mathcal{A}\mu(n) = \kappa_n\int_{w_n^+}^{w_n^-}\cos(2\pi f_0[(u_1\cos\gamma_n+h\sin\psi_n)\cos\alpha_y+(u_1\sin\gamma_n-l-h\cos\psi_n)\sin\alpha_y]w+\lambda_n)dw \tag{21}$$

$$= \frac{\kappa_n\left[\begin{array}{c}\sin(2\pi f_0[(u_1\cos\gamma_n+h\sin\psi_n)\cos\alpha_y+(u_1\sin\gamma_n-l-h\cos\psi_n)\sin\alpha_y]w_n^-+\lambda_n)\\ -\sin(2\pi f_0[(u_1\cos\gamma_n+h\sin\psi_n)\cos\alpha_y+(u_1\sin\gamma_n-l-h\cos\psi_n)\sin\alpha_y]w_n^++\lambda_n)\end{array}\right]}{2\pi f_0[(u_1\cos\gamma_n+h\sin\psi_n)\cos\alpha_y+(u_1\sin\gamma_n-l-h\cos\psi_n)\sin\alpha_y]}, \tag{22}$$

where

$$\kappa_n = C[h\cos(\psi_n-\gamma_n)+l\cos\gamma_n]\sec\theta_n, \tag{23}$$

$$\lambda_n = 2\pi f_0[(l+h\cos\psi_n-z_0)\sin\alpha_y-(h\sin\psi_n+x_0)\cos\alpha_y]. \tag{24}$$

Using a sum-to-product trigonometric identity for real numbers $b_1$ and $b_2$,

$$\sin(b_1)-\sin(b_2) = 2\cos\left(\frac{b_1+b_2}{2}\right)\sin\left(\frac{b_1-b_2}{2}\right). \tag{25}$$

Equation (22) can be rewritten as

$$\begin{aligned}\mathcal{A}\mu(n) = {} & \kappa_n(w_n^- - w_n^+)\mathrm{sinc}(f_0[(u_1\cos\gamma_n+h\sin\psi_n)\cos\alpha_y+(u_1\sin\gamma_n-l-h\cos\psi_n)\sin\alpha_y][w_n^- - w_n^+])\\ & \cdot\cos(\pi f_0[(u_1\cos\gamma_n+h\sin\psi_n)\cos\alpha_y+(u_1\sin\gamma_n-l-h\cos\psi_n)\sin\alpha_y][w_n^+ + w_n^-]+\lambda_n)\end{aligned} \tag{26}$$

$$\begin{aligned}= {} & \left[\frac{\varepsilon\kappa_n\sec\alpha_y}{l+h\cos\psi_n+(u_1\cos\gamma_n+h\sin\psi_n)\tan\alpha_y-u_1\sin\gamma_n}\right]\\ & \cdot\mathrm{sinc}\left(\frac{\varepsilon f_0[u_1\cos\gamma_n+h\sin\psi_n+(u_1\sin\gamma_n-l-h\cos\psi_n)\tan\alpha_y]}{l+h\cos\psi_n+(u_1\cos\gamma_n+h\sin\psi_n)\tan\alpha_y-u_1\sin\gamma_n}\right)\\ & \cdot\cos\left(\frac{\left(\begin{array}{c}2\pi f_0[(u_1\cos\gamma_n+h\sin\psi_n)\cos\alpha_y+(u_1\sin\gamma_n-l-h\cos\psi_n)\sin\alpha_y]\\ \cdot[l+h\cos\psi_n+(x_0+h\sin\psi_n)\tan\alpha_y-z_0]\end{array}\right)}{l+h\cos\psi_n+(u_1\cos\gamma_n+h\sin\psi_n)\tan\alpha_y-u_1\sin\gamma_n}+\lambda_n\right),\end{aligned} \tag{27}$$

where

$$\mathrm{sinc}(u) \equiv \frac{\sin(\pi u)}{\pi u}. \tag{28}$$

Equation (27) gives the signal recorded by the x-ray converter in a detector with no noise or blurring. Lee *et al.*[11] showed that an amorphous selenium (*a*-Se) photoconductor operated in drift mode is a good approximation for an x-ray converter with these characteristics. This photoconductor has a MTF of approximately unity at all frequencies.[11] It is useful to model an *a*-Se detector for the purpose of this work, since this detector is present in the experimental system that is used in Sec. 4 to create oblique reconstructions of a bar pattern phantom. Although it is beyond the scope of this work to model detector noise and blurring, a few strategies for simulating these concepts in futures studies are addressed in Sec. 6.

The digitized signal is now found by sampling the total x-ray attenuation using a thin-film transistor (TFT) array having detector elements with area $a_x \times a_y$. The logarithmically transformed signal in the **m**th detector element for the $n$th projection is

$$\mathcal{D}\mu(\mathbf{m},n) = \int_{a_y m_y}^{a_y(m_y+1)}\int_{a_x(m_x-1/2)}^{a_x(m_x+1/2)}\mathcal{A}\mu(n)\cdot\frac{du_1}{a_x}\frac{du_2}{a_y}, \tag{29}$$

where $m_x$ and $m_y$ are integers used for labeling detector elements. Detector elements are centered on $u_1 = m_x a_x$ and $u_2 = (m_y + 1/2)a_y$. In the case of square detector elements, it is assumed that $a_x = a_y = a$. Although Eq. (29) cannot be evaluated in closed form, this integral can be calculated numerically using the midpoint formula, which is addressed in our previous work.[5]

The attenuation coefficient can now be reconstructed using a filtered backprojection (FBP) formula derived in our previous work.[5] It is important to evaluate the reconstruction using pitched slices with extent in the $\mathbf{i}''$ and $\mathbf{j}''$ directions [Eq. (30)]

$$\begin{pmatrix} x \\ y \\ z \end{pmatrix} = \begin{pmatrix} x_0 \\ y_0 \\ z_0 \end{pmatrix} + \begin{pmatrix} \cos\alpha_y & 0 & -\sin\alpha_y \\ 0 & 1 & 0 \\ \sin\alpha_y & 0 & \cos\alpha_y \end{pmatrix} \begin{pmatrix} x'' \\ y'' \\ z'' \end{pmatrix}. \tag{30}$$

Within this slice, $x''$ measures position along the pitch ($\alpha_y$) and $y''$ measures position perpendicular to the plane of x-ray tube motion. By contrast, $z''$ denotes position perpendicular to the slice. All three positions in the double primed coordinate system are measured relative to the point ($x_0$, $y_0$, $z_0$) in the input object.

Following linear systems theory,[10] the net reconstruction filter should be written as the product of ramp (RA) and spectrum apodization (SA) filters in the Fourier domain. The SA filter is conventionally given by a Hanning window function. The filters are truncated at the frequencies $\pm\xi$ in Fourier space.

### 2.C. Fourier transform of the pitched reconstruction slice

To demonstrate that the input object is resolved in the image, the Fourier transform of the pitched reconstruction plane should have a major peak at the test frequency, $f_0$. The Fourier transform is now calculated analytically using the FBP reconstruction formula that is derived in our previous work [Eq. (65) in Acciavatti and Maidment[5]]

$$\mu_{\mathrm{FBP}}(x,y,z) = \sum_{\mathbf{m},n} \frac{\mathcal{D}\mu(\mathbf{m},n)}{N} \cdot [\rho_1(t_1)]|_{t_1=\sigma_{1\mathbf{m}n}x+\sigma_{2\mathbf{m}n}z} \cdot [\rho_2(t_2)]|_{t_2=\sigma_{3\mathbf{m}n}x+\sigma_{4\mathbf{m}n}y+\sigma_{5\mathbf{m}n}z}. \tag{31}$$

The variables $\rho$ and $\sigma$ were defined in our prior study to simplify intermediate calculations.[5] It was demonstrated in that work that the 1D Fourier transforms ($\mathcal{F}_1$) of $\rho_1$ and $\rho_2$ are

$$\mathcal{F}_1\rho_1(f_1) = \mathcal{F}_1\phi(f_1)\cdot a_x\cos(\theta_{\mathbf{m}n})\mathrm{sinc}(a_x f_1\cos\theta_{\mathbf{m}n}) \cdot e^{-2\pi i m_x a_x f_1\cos\theta_{\mathbf{m}n}} \tag{32}$$

$$\mathcal{F}_1\rho_2(f_2) = a_y\cos(\theta_{\mathbf{m}n})\mathrm{sinc}(a_y f_2\cos\theta_{\mathbf{m}n}) \cdot e^{-2\pi i(m_y+1/2)a_y f_2\cos\theta_{\mathbf{m}n}} \tag{33}$$

where $\mathcal{F}_1\phi(f_1)$ is the Fourier representation of the filter and $\theta_{\mathbf{m}n}$ is the evaluation of $\theta_n$ at the centroid of the $\mathbf{m}$th detector element. Thus, the 2D Fourier transform ($\mathcal{F}_2$) of Eq. (31) within the pitched reconstruction slice at the fixed depth $z''$ is

$$\mathcal{F}_2\mu_{\mathrm{FBP}}(f_x'',f_y'') = \sum_{\mathbf{m},n}\frac{\mathcal{D}\mu(\mathbf{m},n)}{N} \cdot \int_{-\infty}^{\infty}\rho_1(\sigma_{1\mathbf{m}n}x+\sigma_{2\mathbf{m}n}z) \cdot I''_{y\mathbf{m}n}(x,z)\cdot e^{-2\pi i f_x'' x''}dx'', \tag{34}$$

where

$$I''_{y\mathbf{m}n}(x,z) = \int_{-\infty}^{\infty}\rho_2[\sigma_{3\mathbf{m}n}x+\sigma_{4\mathbf{m}n}(y_0+y'')+\sigma_{5\mathbf{m}n}z] \cdot e^{-2\pi i f_y'' y''}dy''. \tag{35}$$

In Eq. (34), the variables $f_x''$ and $f_y''$ are introduced to measure frequency along the $x''$ and $y''$ directions, respectively, within the pitched slice. Equation (35) can be evaluated by making the substitution

$$\eta''_{y\mathbf{m}n} = \sigma_{3\mathbf{m}n}x+\sigma_{4\mathbf{m}n}(y_0+y'')+\sigma_{5\mathbf{m}n}z. \tag{36}$$

Since $\sigma_{4\mathbf{m}n}>0$, one finds

$$I''_{y\mathbf{m}n}(x,z) = \int_{-\infty}^{\infty}\rho_2(\eta''_{y\mathbf{m}n})e^{\frac{-2\pi i f_y''(\eta''_{y\mathbf{m}n}-\sigma_{3\mathbf{m}n}x-\sigma_{5\mathbf{m}n}z-\sigma_{4\mathbf{m}n}y_0)}{\sigma_{4\mathbf{m}n}}}\frac{d\eta''_{y\mathbf{m}n}}{\sigma_{4\mathbf{m}n}} \tag{37}$$

$$= \frac{e^{\frac{2\pi i f_y''(\sigma_{3\mathbf{m}n}x+\sigma_{5\mathbf{m}n}z+\sigma_{4\mathbf{m}n}y_0)}{\sigma_{4\mathbf{m}n}}}}{\sigma_{4\mathbf{m}n}}\int_{-\infty}^{\infty}\rho_2(\eta''_{y\mathbf{m}n})e^{-2\pi i\left(\frac{f_y''}{\sigma_{4\mathbf{m}n}}\right)\eta''_{y\mathbf{m}n}}d\eta''_{y\mathbf{m}n} \tag{38}$$

$$= \frac{e^{\frac{2\pi i f_y''(\sigma_{3\mathbf{m}n}x+\sigma_{5\mathbf{m}n}z+\sigma_{4\mathbf{m}n}y_0)}{\sigma_{4\mathbf{m}n}}}}{\sigma_{4\mathbf{m}n}}\mathcal{F}_1\rho_2\left(\frac{f_y''}{\sigma_{4\mathbf{m}n}}\right). \tag{39}$$

Hence, from Eq. (34), it follows that

$$\mathcal{F}_2\mu_{\mathrm{FBP}}(f_x'',f_y'') = \sum_{\mathbf{m},n}\frac{\mathcal{D}\mu(\mathbf{m},n)}{N}\frac{I''_{x\mathbf{m}n}}{\sigma_{4\mathbf{m}n}}\mathcal{F}_1\rho_2\left(\frac{f_y''}{\sigma_{4\mathbf{m}n}}\right), \tag{40}$$

where

$$I''_{x\mathbf{m}n} = \int_{-\infty}^{\infty}\rho_1(\sigma_{1\mathbf{m}n}x+\sigma_{2\mathbf{m}n}z) \cdot e^{-2\pi i\left[f_x''x''-\frac{(\sigma_{3\mathbf{m}n}x+\sigma_{5\mathbf{m}n}z+\sigma_{4\mathbf{m}n}y_0)f_y''}{\sigma_{4\mathbf{m}n}}\right]}dx'' \tag{41}$$

$$= \int_{-\infty}^{\infty}\rho_1[(\sigma_{1\mathbf{m}n}\cos\alpha_y+\sigma_{2\mathbf{m}n}\sin\alpha_y)x''+\sigma_{1\mathbf{m}n}x_1+\sigma_{2\mathbf{m}n}z_1]\cdot e^{-2\pi i\left[\left(f_x''-\frac{[\sigma_{3\mathbf{m}n}\cos\alpha_y+\sigma_{5\mathbf{m}n}\sin\alpha_y]f_y''}{\sigma_{4\mathbf{m}n}}\right)x''-\frac{(\sigma_{3\mathbf{m}n}x_1+\sigma_{5\mathbf{m}n}z_1+\sigma_{4\mathbf{m}n}y_0)f_y''}{\sigma_{4\mathbf{m}n}}\right]}dx'', \tag{42}$$

and where

$$x_1 = x_0 - z''\sin\alpha_y, \tag{43}$$

$$z_1 = z_0 + z''\cos\alpha_y. \tag{44}$$

Equation (30) justifies the transition from Eq. (41) to Eq. (42). In Eqs. (43) and (44), the variables $x_1$ and $z_1$ are introduced to simplify intermediate calculations. To evaluate Eq. (42), it is necessary to perform the change of variables

$$\eta''_{x\mathbf{m}n} = (\sigma_{1\mathbf{m}n}\cos\alpha_y + \sigma_{2\mathbf{m}n}\sin\alpha_y)x'' + \sigma_{1\mathbf{m}n}x_1 + \sigma_{2\mathbf{m}n}z_1, \tag{45}$$

giving

$$I''_{x\mathbf{m}n} = \int_{-\infty}^{\infty} \rho_1(\eta''_{x\mathbf{m}n}) e^{-2\pi i\left[\left(f''_x - \frac{[\sigma_{3\mathbf{m}n}\cos\alpha_y + \sigma_{5\mathbf{m}n}\sin\alpha_y]f''_y}{\sigma_{4\mathbf{m}n}}\right)\left(\frac{\eta''_{x\mathbf{m}n} - \sigma_{1\mathbf{m}n}x_1 - \sigma_{2\mathbf{m}n}z_1}{\sigma_{1\mathbf{m}n}\cos\alpha_y + \sigma_{2\mathbf{m}n}\sin\alpha_y}\right) - \frac{(\sigma_{3\mathbf{m}n}x_1 + \sigma_{5\mathbf{m}n}z_1 + \sigma_{4\mathbf{m}n}y_0)f''_y}{\sigma_{4\mathbf{m}n}}\right]} \frac{d\eta''_{x\mathbf{m}n}}{|\sigma_{1\mathbf{m}n}\cos\alpha_y + \sigma_{2\mathbf{m}n}\sin\alpha_y|} \tag{46}$$

$$= \frac{e^{2\pi i\left[\left(f''_x - \frac{[\sigma_{3\mathbf{m}n}\cos\alpha_y + \sigma_{5\mathbf{m}n}\sin\alpha_y]f''_y}{\sigma_{4\mathbf{m}n}}\right)\left(\frac{\sigma_{1\mathbf{m}n}x_1 + \sigma_{2\mathbf{m}n}z_1}{\sigma_{1\mathbf{m}n}\cos\alpha_y + \sigma_{2\mathbf{m}n}\sin\alpha_y}\right) + \frac{(\sigma_{3\mathbf{m}n}x_1 + \sigma_{5\mathbf{m}n}z_1 + \sigma_{4\mathbf{m}n}y_0)f''_y}{\sigma_{4\mathbf{m}n}}\right]}}{|\sigma_{1\mathbf{m}n}\cos\alpha_y + \sigma_{2\mathbf{m}n}\sin\alpha_y|} \int_{-\infty}^{\infty} \rho_1(\eta''_{x\mathbf{m}n}) e^{-2\pi i\left(\frac{\sigma_{4\mathbf{m}n}f''_x - [\sigma_{3\mathbf{m}n}\cos\alpha_y + \sigma_{5\mathbf{m}n}\sin\alpha_y]f''_y}{\sigma_{4\mathbf{m}n}[\sigma_{1\mathbf{m}n}\cos\alpha_y + \sigma_{2\mathbf{m}n}\sin\alpha_y]}\right)\eta''_{x\mathbf{m}n}} d\eta''_{x\mathbf{m}n} \tag{47}$$

$$= \frac{e^{2\pi i\left[\left(f''_x - \frac{[\sigma_{3\mathbf{m}n}\cos\alpha_y + \sigma_{5\mathbf{m}n}\sin\alpha_y]f''_y}{\sigma_{4\mathbf{m}n}}\right)\left(\frac{\sigma_{1\mathbf{m}n}x_1 + \sigma_{2\mathbf{m}n}z_1}{\sigma_{1\mathbf{m}n}\cos\alpha_y + \sigma_{2\mathbf{m}n}\sin\alpha_y}\right) + \frac{(\sigma_{3\mathbf{m}n}x_1 + \sigma_{5\mathbf{m}n}z_1 + \sigma_{4\mathbf{m}n}y_0)f''_y}{\sigma_{4\mathbf{m}n}}\right]}}{|\sigma_{1\mathbf{m}n}\cos\alpha_y + \sigma_{2\mathbf{m}n}\sin\alpha_y|} \mathcal{F}_1\rho_1\left(\frac{\sigma_{4\mathbf{m}n}f''_x - [\sigma_{3\mathbf{m}n}\cos\alpha_y + \sigma_{5\mathbf{m}n}\sin\alpha_y]f''_y}{\sigma_{4\mathbf{m}n}(\sigma_{1\mathbf{m}n}\cos\alpha_y + \sigma_{2\mathbf{m}n}\sin\alpha_y)}\right). \tag{48}$$

Substituting Eq. (48) into Eq. (40) yields the final expression for the 2D Fourier transform

$$\mathcal{F}_2\mu_{\mathrm{FBP}}(f''_x, f''_y) = \sum_{\mathbf{m},n} \frac{\mathcal{D}\mu(\mathbf{m},n)}{N} \frac{e^{2\pi i\left[\left(f''_x - \frac{[\sigma_{3\mathbf{m}n}\cos\alpha_y + \sigma_{5\mathbf{m}n}\sin\alpha_y]f''_y}{\sigma_{4\mathbf{m}n}}\right)\left(\frac{\sigma_{1\mathbf{m}n}x_1 + \sigma_{2\mathbf{m}n}z_1}{\sigma_{1\mathbf{m}n}\cos\alpha_y + \sigma_{2\mathbf{m}n}\sin\alpha_y}\right) + \frac{(\sigma_{3\mathbf{m}n}x_1 + \sigma_{5\mathbf{m}n}z_1 + \sigma_{4\mathbf{m}n}y_0)f''_y}{\sigma_{4\mathbf{m}n}}\right]}}{|\sigma_{1\mathbf{m}n}\cos\alpha_y + \sigma_{2\mathbf{m}n}\sin\alpha_y|\sigma_{4\mathbf{m}n}}$$

$$\cdot \mathcal{F}_1\rho_1\left(\frac{\sigma_{4\mathbf{m}n}f''_x - [\sigma_{3\mathbf{m}n}\cos\alpha_y + \sigma_{5\mathbf{m}n}\sin\alpha_y]f''_y}{\sigma_{4\mathbf{m}n}\left(\sigma_{1\mathbf{m}n}\cos\alpha_y + \sigma_{2\mathbf{m}n}\sin\alpha_y\right)}\right)\mathcal{F}_1\rho_2\left(\frac{f''_y}{\sigma_{4\mathbf{m}n}}\right). \tag{49}$$

An important special case of Eq. (49) occurs with $f''_y = 0$

$$\mathcal{F}_2\mu_{\mathrm{FBP}}(f''_x, 0) = \sum_{\mathbf{m},n} \frac{\mathcal{D}\mu(\mathbf{m},n)}{N} \frac{e^{\frac{2\pi i[\sigma_{1\mathbf{m}n}(x_0 - z''\sin\alpha_y) + \sigma_{2\mathbf{m}n}(z_0 + z''\cos\alpha_y)]f''_x}{\sigma_{1\mathbf{m}n}\cos\alpha_y + \sigma_{2\mathbf{m}n}\sin\alpha_y}} a_y\cos\theta_{\mathbf{m}n}}{|\sigma_{1\mathbf{m}n}\cos\alpha_y + \sigma_{2\mathbf{m}n}\sin\alpha_y|\sigma_{4\mathbf{m}n}} \mathcal{F}_1\rho_1\left(\frac{f''_x}{\sigma_{1\mathbf{m}n}\cos\alpha_y + \sigma_{2\mathbf{m}n}\sin\alpha_y}\right). \tag{50}$$

This special case is useful for analyzing an input frequency oriented along the pitch, $\alpha_y$, such as the input frequency given in Eq. (2). To analyze an input frequency oriented along a 0° pitch ($\alpha_y = 0$), one can introduce the equation $z = z_0$ to define the plane of reconstruction. It follows directly from Eqs. (1) and (30) that the following properties hold for this reconstruction plane: $x_0 = z'' = 0$ and $f''_x = f_x$. If one makes these substitutions in Eq. (50), one can recover the Fourier transform of a conventional reconstruction plane that was derived in our previous work [Eq. (86) in Acciavatti and Maidment[5]]. This agreement with our previous work provides a built-in check on the validity of Eq. (50).

## 3. THEORETICAL RESULTS

### 3.A. Projection images

Projection images are now simulated for a Selenia Dimensions DBT system (Hologic, Inc., Bedford, MA), assuming an object thickness ($\varepsilon$) of 0.05 mm, an object pitch ($\alpha_y$) of 20°, and an object displacement ($x_0$) of 0 mm along the direction parallel to the chest wall side of the breast support. The object thickness was chosen based on the size of a small calcification in breast imaging. The acquisition parameters for the system are detailed in our previous work.[5] The centroid of the sine plate (point D in Fig. 1) is simulated at the depth $z_0 = 50.0$ mm. This depth corresponds to the mid-thickness of a typical breast size (50.0 mm thick), assuming that the breast support is 25.0 mm above the detector. In order to investigate super-resolution in this system with 140 $\mu$m detector elements, the test frequency ($f_0$) is chosen to be 5.0 lp/mm. This input frequency is higher than the detector alias frequency (3.6 lp/mm).

The total attenuation of a zero frequency object is now calculated in order to normalize the amplitude $C$ of the attenuation coefficient of the input waveform. From Eqs. (23) and (27), it follows that

$$C = \left[\frac{1}{N}\sum_n \frac{\varepsilon[h\cos(\psi_n - \gamma_n) + l\cos\gamma_n]\sec(\theta_n)\sec(\alpha_y)}{l + h\cos\psi_n + [u_1(n)\cos\gamma_n + h\sin\psi_n]\tan\alpha_y - u_1(n)\sin\gamma_n}\right]^{-1}, \tag{51}$$

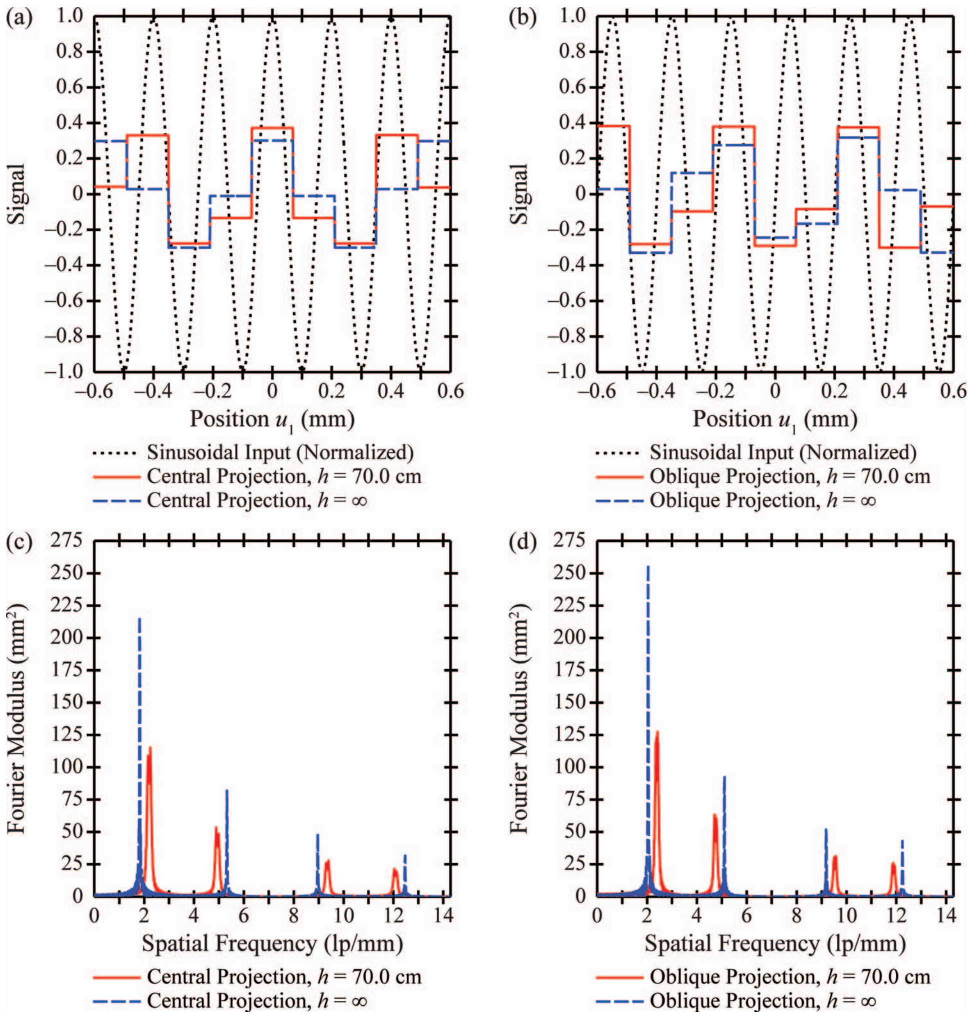


FIG. 2. (a) and (b) Two projection images of a pitched sine plate are shown, assuming $\alpha_y = 20^\circ, f_0 = 5.0$ lp/mm, $\varepsilon = 0.05$ mm, $x_0 = 0$ mm, and $z_0 = 50.0$ mm. Signal is plotted versus detector position $u_1$ at the fixed distance ($u_2$) of 30.0 mm from the plane of x-ray tube motion. The presence of each detector element ($a = 0.14$ mm) is modeled by a rectangle function. (c) and (d) The Fourier transforms of each projection show classical signs of aliasing. The major Fourier peak does not occur at the input frequency (5.0 lp/mm) but instead at a frequency less than the detector alias frequency, 3.6 lp/mm.

where

$$u_1(n) = \frac{x_0(l + h\cos\psi_n) + z_0 h \sin\psi_n}{x_0 \sin\gamma_n + (l - z_0)\cos\gamma_n + h\cos(\psi_n - \gamma_n)}, \tag{52}$$

$$u_2(n) = \frac{y_0[l\cos\gamma_n + h\cos(\psi_n - \gamma_n)]}{x_0 \sin\gamma_n + (l - z_0)\cos\gamma_n + h\cos(\psi_n - \gamma_n)}. \tag{53}$$

This calculation assumes that rays for each projection pass through the point $(x_0, y_0, z_0)$, giving rise to x-ray attenuation. Concordant with our previous work, Eqs. (52) and (53) are derived from the equations [Eqs. (11)–(13)] for the ray between the focal spot and the point $(u_1, u_2)$ on the detector. Although $u_2(n)$ is not a coordinate listed directly in Eq. (51), it is calculated in Eq. (53) as a necessary substitution in the formula for $\theta_n$ [Eq. (20)].

In Figs. 2(a) and 2(b), a cross section of signal is plotted versus detector position $u_1$ for the central projection ($n = 0$) and an oblique projection ($n = 7$). The signal is calculated at the distance $u_2 = 30.0$ mm from the chest wall side of the breast support. Following our previous work,[5] this $u_2$ displacement is chosen to simulate a position approximately halfway between the chest wall and nipple in a typical breast size (450 ml). To illustrate that oblique x-ray incidence introduces a translational shift in the image of the object on the detector, Fig. 2(b) shows the shift in the oblique projection [Eq. (52)], assuming that $h = 70.0$ cm as would be characteristic of the Selenia Dimensions system. The analogous shift in the central projection is zero [Fig. 2(a)].

Although detector signal is a discrete function in a digital system, it is represented graphically as a continuous function in Figs. 2(a) and 2(b). The presence of each detector element is modeled by a rectangle function whose width matches the detector element length (0.14 mm). The projection images do not have the appearance of the input waveform, but instead are step-like due to the detector element sampling.

To illustrate the presence of aliasing in the two projection images, the Fourier transform of detector signal is also

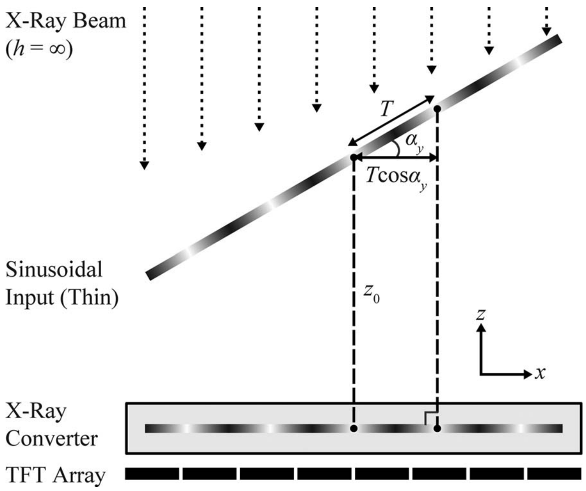


FIG. 3. The projection of a pitched sine plate onto the detector is illustrated using a parallel x-ray beam geometry ($h = \infty$). As shown, the period $T$ of the input waveform is projected onto the x-ray converter as $T\cos\alpha_y$ in the central projection. Hence, the frequency detected by the x-ray converter is $f_0 \sec\alpha_y$, or 5.3 lp/mm assuming $f_0 = 5.0$ lp/mm and $\alpha_y = 20°$. This frequency corresponds to the first minor Fourier peak in Fig. 2(c) in the acquisition geometry for which $h = \infty$.

calculated in Fig. 2. Our previous study has demonstrated that this Fourier transform is

$$\mathcal{F}_2(\mathcal{S}\mu)(f_1, f_2) = a^2 \text{sinc}(af_1)\text{sinc}(af_2) \cdot \sum_{\mathbf{m}} \mathcal{D}\mu(\mathbf{m}, n) \cdot e^{-2\pi i a[m_x f_1 + (m_y + 1/2) f_2]}, \tag{54}$$

where $\mathcal{S}\mu$ denotes the detector signal, and $f_1$ and $f_2$ measure frequency along the $u_1$ and $u_2$ directions, respectively. Figures 2(c) and 2(d) show the Fourier transform versus $f_1$, assuming $f_2 = 0$. The major peak of the Fourier transform does not occur at the input frequency (5.0 lp/mm), but instead at a frequency less than the detector alias frequency (3.6 lp/mm). This finding is concordant with our prior work studying a similar test frequency at a 0° pitch in place of the 20° pitch.

Although the source-to-COR distance ($h$) is 70.0 cm in the Selenia Dimensions system, it is useful to consider projections at an infinite value of $h$. This limiting case corresponds to a parallel-beam geometry. As illustrated in Figs. 2(c) and 2(d), the positions of the Fourier peaks for each projection are dependent on $h$. For a parallel-beam geometry ($h = \infty$), Fig. 3 illustrates how to calculate the frequencies of the Fourier peaks in the central projection. The period $T$ of the test frequency projects onto the x-ray converter as $T\cos\alpha_y$. Hence, the projected frequency is $f_0 \sec\alpha_y$, or 5.3 lp/mm. This frequency gives the first minor Fourier peak in Fig. 2(c). Sampling by the TFT array aliases the input frequency to 1.8 lp/mm, yielding the major Fourier peak. The two largest Fourier peaks in Fig. 2(c) are equidistant from the detector alias frequency $0.5a^{-1}$ (3.6 lp/mm). As shown in the figure, two additional Fourier peaks occur at 9.0 and 12.5 lp/mm. These peaks are similarly equidistant from the frequency $1.5a^{-1}$ (10.7 lp/mm).

Unlike a parallel-beam geometry, a divergent-beam geometry ($h = 70.0$ cm) magnifies the object that is projected onto the x-ray converter. Denoting $M$ as the magnification

$$M = \frac{h}{h - z_0}, \tag{55}$$

it follows from Fig. 3 that the test frequency $f_0$ projects onto the x-ray converter as $M^{-1} \cdot f_0 \sec\alpha_y$, or 4.9 lp/mm. This frequency corresponds to the first minor Fourier peak in Fig. 2(c). The major peak at 2.2 lp/mm and the first minor peak are equidistant from the alias frequency, 3.6 lp/mm. As expected, additional Fourier peaks occur at 9.3 and 12.1 lp/mm with equal distance relative to the frequency $1.5a^{-1}$ (10.7 lp/mm).

### 3.B. SBP and FBP reconstruction

In Fig. 4(a), SBP reconstruction is shown in a slice with signal measured in the $x''$ direction along a 20° pitch, assuming that $y'' = 0$ and $z'' = 0$ [Eq. (30)]. Although a single projection is not capable of resolving the test frequency, the pitched reconstruction is capable of resolving 5.0 lp/mm properly. The corresponding SBP Fourier transform [Eq. (50)] shows that the major peak occurs at the input frequency [Fig. 4(c)]. These results generalize our previous work on super-resolution at a 0° pitch to an oblique pitch.

FBP reconstructions and their Fourier transforms are also plotted in Fig. 4 using either the RA filter alone or the RA and SA filters together. Following our previous work on super-resolution,[5] the filter truncation frequency ($\xi$) is 14.3 lp/mm, corresponding to the second zero of the MTF of the detector sampling process

$$\text{MTF}(f_1, f_2) = |\text{sinc}(af_1)\text{sinc}(af_2)|. \tag{56}$$

This value of $\xi$ is chosen to correspond with the second zero of the MTF measured along the $f_1$ direction, assuming that $f_2 = 0$. Figure 4 demonstrates that like SBP, the Fourier transforms of FBP reconstructions possess their major peak at the input frequency, 5.0 lp/mm. Filtering provides an improvement over SBP reconstruction by smoothing pixelation artifacts in the spatial domain. The two FBP reconstructions differ in that reconstruction with the RA filter alone has greater modulation than reconstruction with the RA and SA filters together. This finding is expected, since the SA filter places more relative weight on low frequencies to reduce high frequency noise. The drawback of reconstructing with the RA filter alone is the increased amplitude of high frequency spectral leakage in the Fourier domain. Figures 4(b) and 4(d) are qualitatively concordant with the results at a 0° pitch in our previous work.

### 3.C. Effect of object thickness on the MTF

Section 3.B has demonstrated the existence of super-resolution in oblique reconstructions using a relatively thin input object ($\varepsilon = 0.05$ mm). Based on our earlier work modeling a non-pixelated detector, one would expect the MTF in an oblique reconstruction to be substantially degraded at large

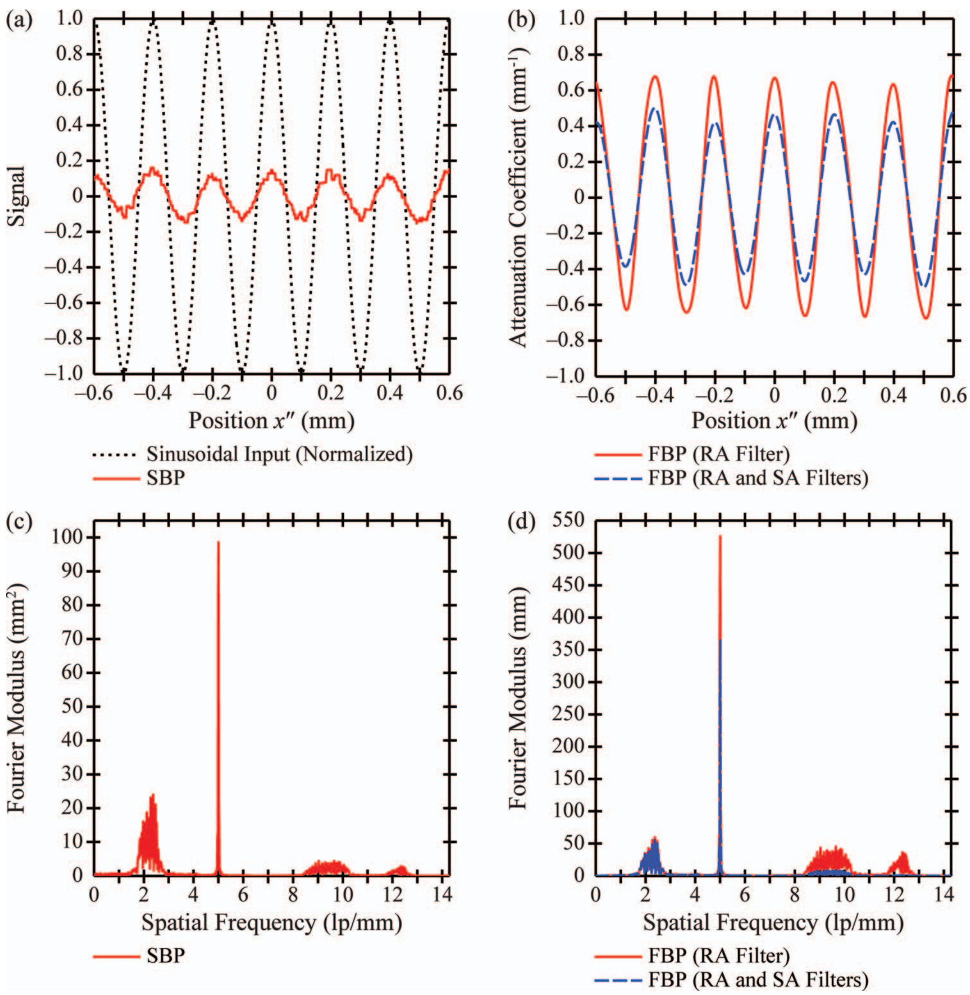


FIG. 4. (a)–(d) SBP and FBP reconstructions are performed using a slice with signal measured in the $x''$ direction along the 20° pitch of the input object, assuming $y'' = 0$ and $z'' = 0$. Unlike a single projection (Fig. 2), the reconstructions can resolve the high frequency object. The corresponding Fourier transforms have a major peak at the input frequency (5.0 lp/mm), demonstrating that our earlier work on super-resolution at a 0° pitch can be generalized to oblique reconstructions.

object thicknesses. For this reason, we now investigate the thickness dependency of super-resolution in oblique reconstructions.

In Fig. 5, the dependency of the MTF on object thickness and frequency is investigated with surface plots at two pitches (0° and 20°), assuming SBP reconstruction. Following convention, the MTF is found by normalizing the amplitude of the reconstruction at each test frequency $f_0$ against the corresponding value for a zero-frequency object ($f_0 = 0$). As Fig. 4 illustrates, the amplitude of the reconstruction can be determined by the value at $x'' = 0$, corresponding to signal at the point ($x_0$, $y_0$, $z_0$).

It is common practice to assume that the detectability limit occurs with a MTF of 10.0%.[12] This threshold is denoted by a solid black line in both subplots of Fig. 5. If the object is very thin ($\varepsilon = 0.01$ mm), one can show that frequencies up to 5.7 and 5.4 lp/mm are detectable at the 0° and 20° pitches, respectively. These frequencies exceed the detector alias frequency, 3.6 lp/mm. Consequently, super-resolution is achievable at either pitch.

Turning next to the case of a thick object, Fig. 5 shows that the MTF is more sharply degraded with increasing frequency. The resolution loss at high frequencies is much more pronounced at the 20° pitch than at the 0° pitch. For example, if the object is 1.0 mm thick, the highest detectable frequencies at the 0° and 20° pitches are 5.4 and 2.5 lp/mm, respectively, assuming that the limit of resolution is a MTF of 10.0%. This finding illustrates that super-resolution is only achievable in an oblique reconstruction if the object is thin. Super-resolution is feasible at a 0° pitch over a much broader range of object thicknesses.

In the reconstruction of a thick object, Fig. 5 demonstrates that low frequencies have detectable modulation over a broader range of pitches than high frequencies. To illustrate this concept, Fig. 6 shows the reconstruction of a relatively thick object ($\varepsilon = 1.0$ mm) at 2.0 and 5.0 lp/mm with either the 0° or 20° pitch. Modulation is detectable at both pitches for the low frequency object, but is detectable only at the 0° pitch for the high frequency object.

In Fig. 6(b), the reconstruction of the 5.0 lp/mm frequency at a 20° pitch shows a 180° phase shift that is not observed in the other plots in the figure. This result can be explained from the fact that the optical transfer function (OTF) is negative. Recall that the MTF is the normalized modulus of the OTF.

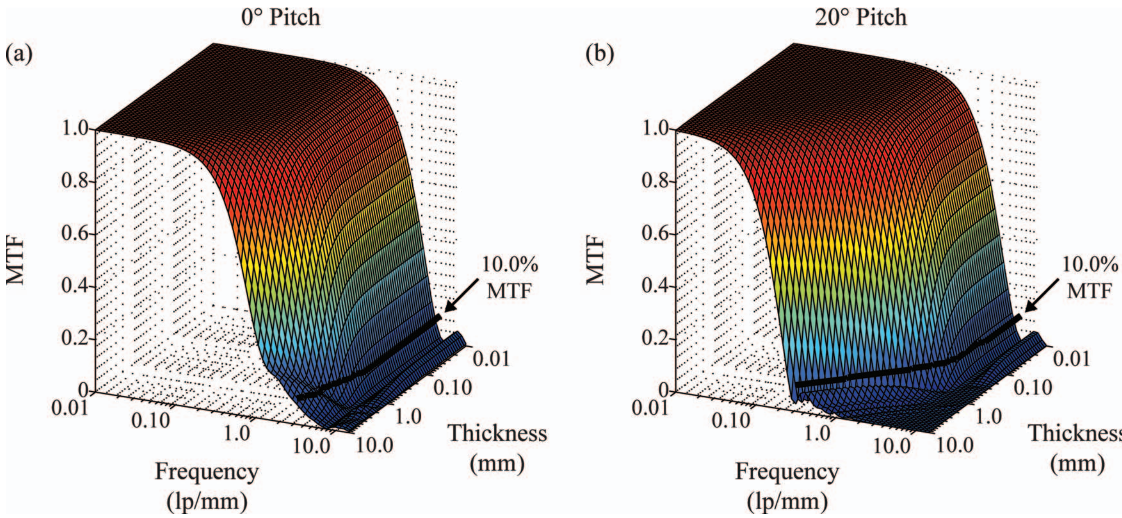


FIG. 5. Using SBP reconstruction, the dependency of the MTF on frequency and object thickness is investigated at two pitches: (a) 0° and (b) 20°. The MTF decreases with frequency, as expected. If the object is thick, the resolution loss at high frequencies is much more pronounced at the 20° pitch than at the 0° pitch.

The OTF attains negative values at frequencies just exceeding the first zero of the MTF (Fig. 5).

### 3.D. Limiting resolution of an oblique reconstruction

#### 3.D.1. Loss of resolution with increasing object thickness

Using a MTF of 10.0% as the limit of resolution, Fig. 6(c) explicitly studies the thickness dependence of the highest frequency with detectable modulation. As expected, it is demonstrated that modulation is within detectable limits over a broad range of frequencies if the object is thin. Modulation is detectable over a narrower range of frequencies if the object is thick.

It is also shown in Fig. 6(c) that the highest frequency with detectable modulation decreases with pitch. If the object is very thin (0.01 mm thick), the highest frequencies with detectable modulation are 5.7, 5.5, 5.0, 4.0, 2.9, and 1.5 lp/mm at 0°, 15°, 30°, 45°, 60°, and 75° pitches, respectively. As expected, the highest frequency with detectable modulation does not exceed the frequency corresponding to 10.0% detector MTF (6.5 lp/mm), which can be calculated from Eq. (56) assuming that $f_2 = 0$. Figure 6(c) illustrates that super-resolution is not achievable at pitches approaching 90°, regardless of object thickness. However, modulation of lower frequency objects is preserved even at high obliquity.

#### 3.D.2. Aliasing at large object thicknesses

In Fig. 6(c), the thickness range is truncated at an intermediate value (3.8 mm) for the 0° pitch. Unlike the other pitches in the plot, it can be demonstrated that frequencies exceeding the detector alias frequency have detectable modulation at thicknesses exceeding 3.8 mm. We now show that these high frequencies are aliased based on a metric developed in our previous work.[5] Using the Fourier transform of the SBP reconstruction of a sine plate [Fig. 4(c)], this metric is the ratio ($r$) of the amplitude of the highest peak less than the detector alias frequency (3.6 lp/mm) to the amplitude at the input frequency (5.0 lp/mm). Super-resolution is present if $r < 1$, while aliasing is present if $r \geq 1$. Figure 6(d) shows that the $r$-factor exceeds unity at thicknesses greater than 3.8 mm for a 0° pitch. Because Fig. 6(d) demonstrates the existence of aliasing at these thicknesses, the corresponding thickness range is truncated in Fig. 6(c).

To further illustrate that aliasing is present at thicknesses exceeding 3.8 mm, the SBP reconstruction of a 5.0 mm thick sine plate is shown in Fig. 7 for the 0° pitch. As expected from Fig. 6(d), this object is not resolved since the peaks and troughs in the reconstruction do not properly match the input frequency. The $r$-factor is 2.0 at this thickness.

### 3.E. Depth-dependence of super-resolution

Using the $r$-factor, our previous work showed that the existence of super-resolution is dependent on depth ($z_0$) in the reconstruction. For frequency measurements along the $x$ direction, it was demonstrated that various depths in the plane $x = 0$ do not exhibit super-resolution. The plane $x = 0$ was termed the mid posteroanterior (PA)/source-to-support (SS) plane in our previous work, since this plane has extent in the PA and SS directions in breast applications. Figure 8 investigates whether the depth-dependency of the $r$-factor continues to hold in oblique reconstructions. The detector field-of-view (FOV) used for calculating the Fourier transforms is $42.1 \times 42.1$ mm and is centered on the mid PA/SS plane. The detector element indices $m_x$ and $m_y$ range from $-150$ to $+150$ and 0 to 301, respectively; this range matches the one used in Fig. 6(d). At the two smallest pitches investigated in Fig. 8 (0° and 2.5°), $r$ exceeds unity at eight depths, which are comparable to the results presented in our earlier work.[5] At these eight peaks, the image of the sine plate is translated in approximately integer multiples of detector element length between projections. Super-resolution is not achievable since

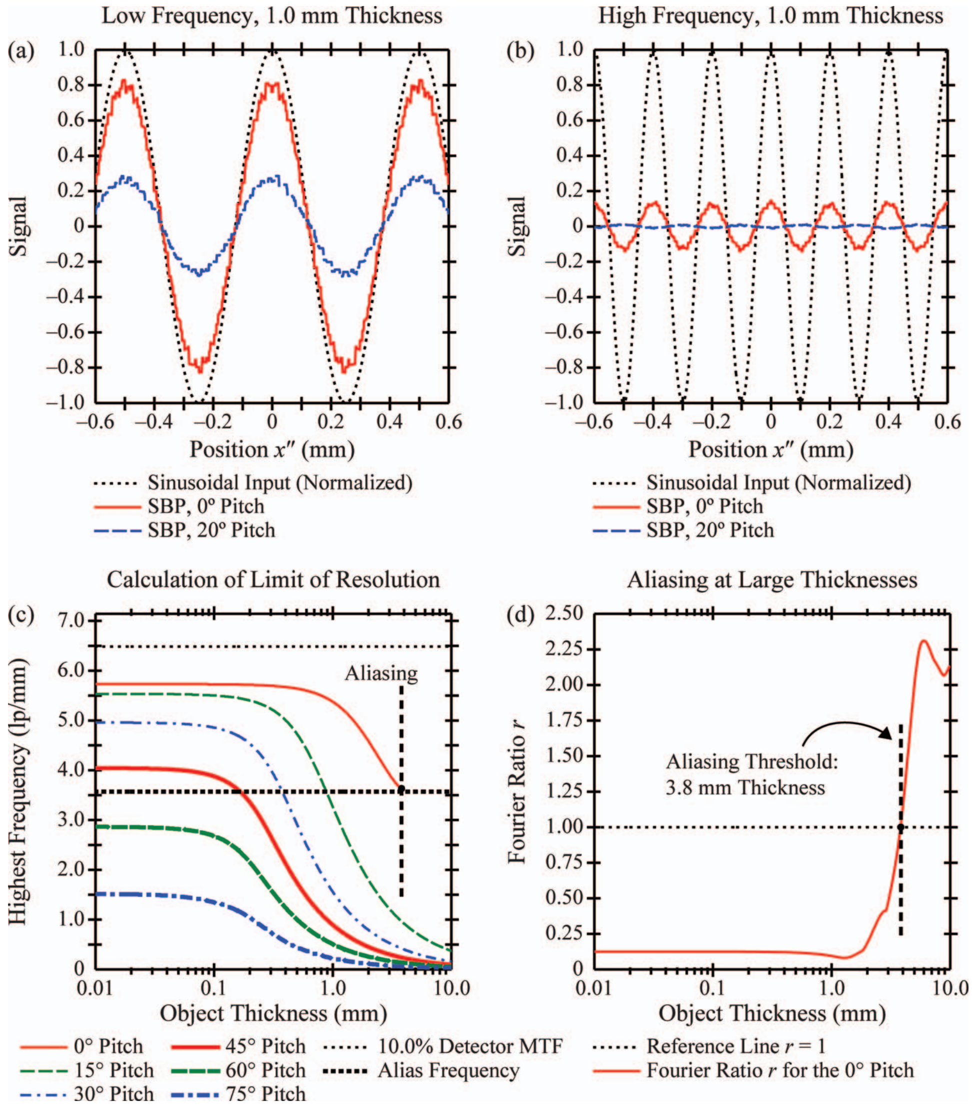


FIG. 6. (a) In the SBP reconstruction of a 1.0 mm thick object with a 2.0 lp/mm input frequency, modulation is detectable at both the 0° and 20° pitches. (b) In the analogous reconstruction at a 5.0 lp/mm input frequency, modulation is detectable only at the 0° pitch. (c) Using a MTF threshold of 10.0% as the limit of resolution of SBP reconstruction, the highest frequency with detectable modulation is plotted versus object thickness. At various pitches, this figure shows that the object must be thin in order to maximize the range of frequencies with detectable modulation. (d) At a 0° pitch, super-resolution is not achievable at thicknesses exceeding 3.8 mm ($r \geq 1$).

the translational shifts between projections do not maximize subpixel sampling gain.

Turning next to the 5.0° pitch, Fig. 8 shows that the $r$-factor continues to peak at eight depths in the reconstruction, but does not exceed unity. Super-resolution is technically achievable at all depths in the reconstruction. Since $r$ exceeds 0.5 at these eight peaks, the quality of super-resolution is not optimal.

By increasing the pitch further to 7.5°, 10.0°, or 20.0°, Fig. 8 shows that the peaks in the value of $r$ have much lower amplitude. Hence, super-resolution with reasonably good quality can be achieved at all depths for these pitches. Although the $r$-factor can be used to analyze the existence of super-resolution, it does not demonstrate whether modulation is within detectable limits. Future work will further explore the calculation of modulation at various reconstruction depths.

## 4. EXPERIMENTAL RESULTS

In order to validate the analytical model, a goniometry stand was used to vary the pitch of a relatively thin ($\varepsilon = 0.05$ mm) bar pattern phantom (Model 07-515, Fluke Biomedical, Cleveland, OH). Projection images were acquired on a Selenia Dimensions DBT system, and reconstruction was performed in the oblique plane of the bar patterns using a commercial prototype backprojection filtering (BPF) algorithm[9] (Briona™, Real Time Tomography, Villanova, PA). The technique factors of the image acquisition matched the ones given in our previous work.[5] The long axis of the phantom, which was centered on the mid PA/SS plane, was positioned at a fixed depth, $z_0 = 10.8$ cm above the detector, for all pitches. Although this depth corresponds to a position outside the breast in a typical 5.0 cm thickness under compression, it was the only depth supported by the

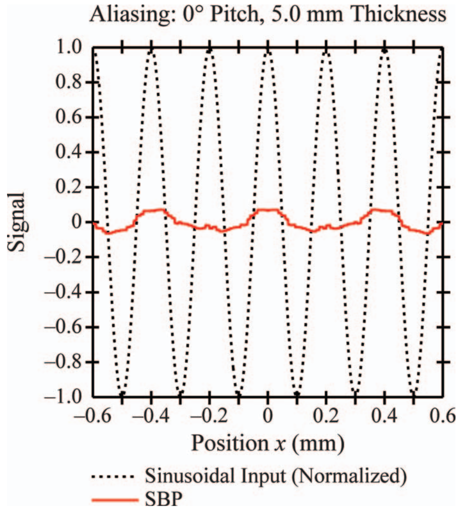


FIG. 7. At a 0° pitch, the SBP reconstruction of a very thick object ($\varepsilon = 5.0$ mm) shows aliasing for a 5.0 lp/mm input frequency. This result illustrates that the thickness of the test object places a constraint on the feasibility of super-resolution, as expected from Fig. 6(d) using the $r$-factor.

goniometry stand and is presented for the purpose of experimental validation of oblique reconstructions.

To illustrate that a single projection image cannot resolve frequencies exceeding the detector alias frequency, the central projection of the bar pattern phantom at a 0° pitch is shown in Fig. 9. The projection misrepresents frequencies higher than 3.6 lp/mm. For example, at 4.0 lp/mm, Moiré patterns are present. At 5–7 lp/mm, the line pairs have an erroneous orientation and are imaged as if they were a lower frequency.

As expected from our earlier work on super-resolution, a reconstruction at a 0° pitch [Fig. 10(a)] is capable of resolving higher frequencies than a single projection. Frequencies up to 5.75 lp/mm can be resolved. This estimate of the highest detectable frequency is approximated to the nearest multiple of 0.25 lp/mm, since it is determined by visual inspection. The reconstruction grid was specified to have ten times smaller pixelation (14.0 $\mu$m) than the detector in order to support super-resolution. At a 30° pitch, the reconstruction in the plane of the bar patterns [Fig. 10(b)] also shows super-resolution, as frequencies up to 4.75 lp/mm have detectable modulation. This experimental result verifies that our earlier work on super-resolution can be generalized to an oblique reconstruction plane.

Concordant with the analytical model, the experimental images demonstrated that super-resolution is not achievable at pitches approaching 90°. To illustrate this concept, Fig. 10(c) shows the reconstruction of the bar pattern phantom at a 60° pitch. The highest frequency with detectable modulation is 3.0 lp/mm.

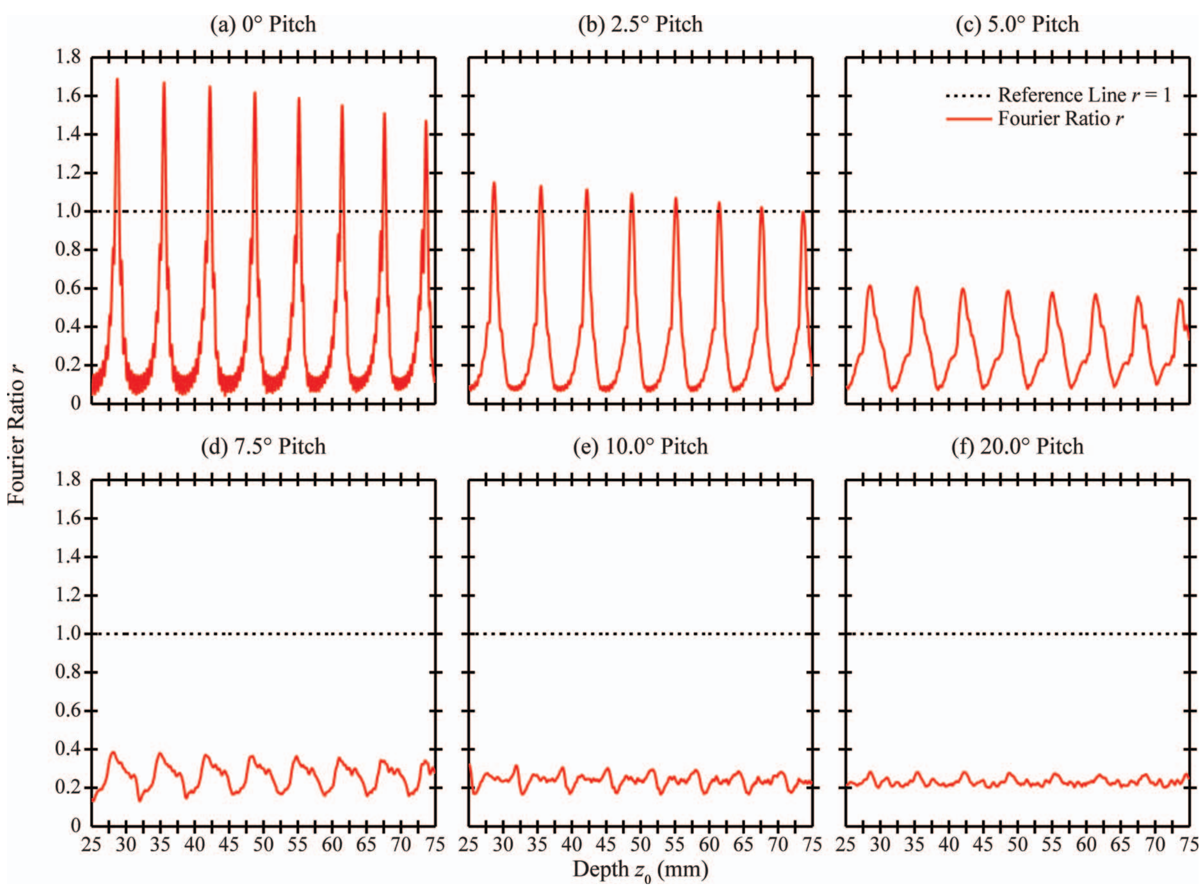


FIG. 8. The depth dependency of super-resolution is investigated for measurements made in the mid PA/SS plane ($x = 0$) using a 5.0 lp/mm input frequency. At a (a) 0° or (b) 2.5° pitch, super-resolution is not achievable at various reconstruction depths for which $r \geq 1$. By increasing the pitch, it is demonstrated that the peaks in the value of $r$ have much lower amplitude: (c) 5.0°, (d) 7.5°, (e) 10.0°, (f) 20.0° pitch. For high quality super-resolution, $r$ should approach zero. All subplots in this figure implicitly share a common legend.

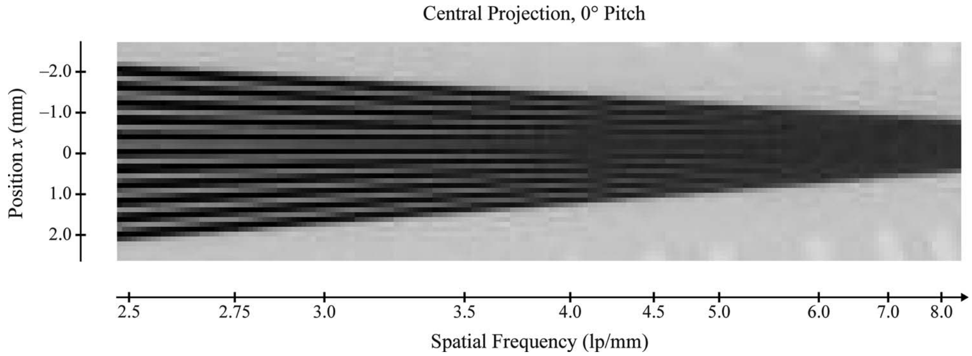


FIG. 9. A bar pattern phantom was positioned parallel to the breast support (i.e., at a 0° pitch) of a Selenia Dimensions DBT system. It is shown here that the central projection cannot resolve frequencies higher than the detector alias frequency, 3.6 lp/mm, for 140 $\mu$m detector elements.

Although Fig. 10 only shows reconstructions at 0°, 30°, and 60° pitches, images of bar patterns at additional pitches were also obtained experimentally. By visually inspecting the reconstruction at each pitch, the highest frequency with detectable modulation was determined. The estimate was approximated to the nearest multiple of 0.25 lp/mm. In Fig. 11, these results are compared against the predictions of the analytical model. Because there is no absolute threshold for detectable modulation, we consider MTF thresholds of 5.0%, 10.0%, and 15.0% in the analytical model. Figure 11 demonstrates that the highest frequency with detectable modulation decreases with pitch. In order to model the mid-thickness of a typical breast size under compression, the analytical results are simulated at a different depth ($z_0 = 5.0$ cm) than the experimental results ($z_0 = 10.8$ cm). The experimental results correspond to a depth exceeding a typical breast size, as this was the only depth supported by the goniometry stand.

In order to demonstrate that the experimental and analytical results follow the same trend with increasing pitch,

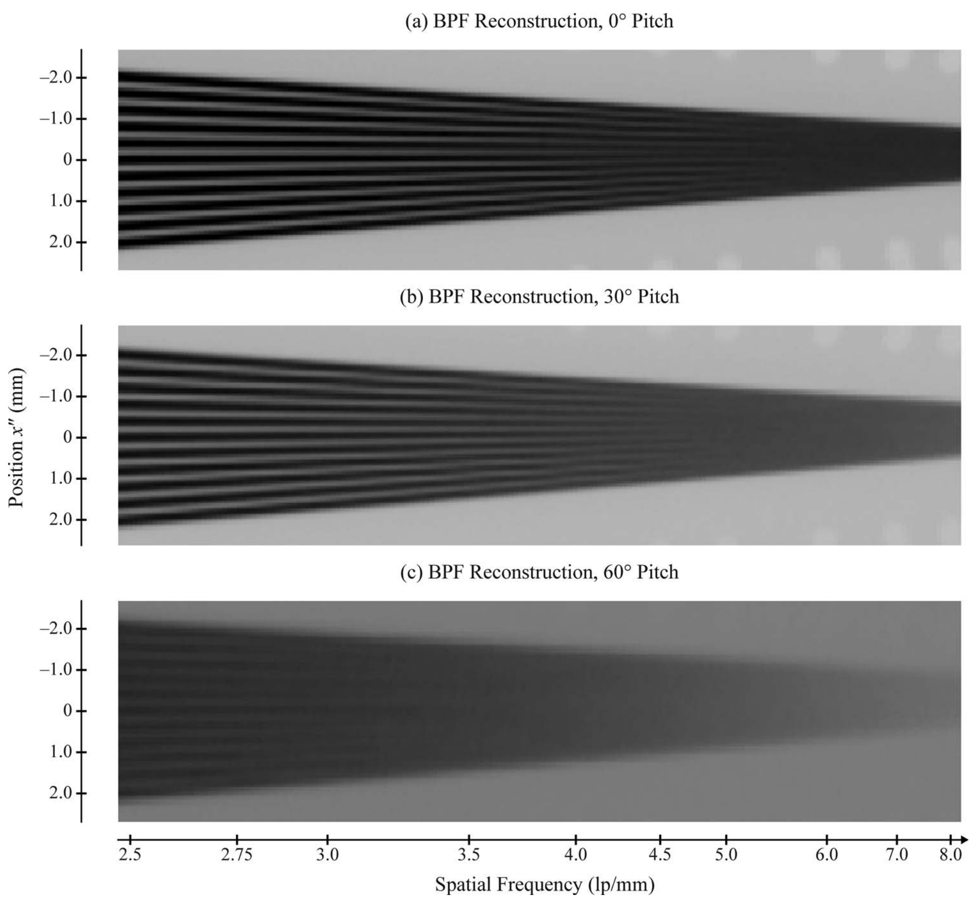


FIG. 10. (a) A BPF reconstruction, which is performed on a grid with much smaller pixelation than the detector, is capable of resolving higher frequencies than a single projection. As shown here at the 0° pitch, the highest frequency with detectable modulation is approximately 5.75 lp/mm. This frequency is higher than the detector alias frequency, 3.6 lp/mm. (b) A reconstruction in the oblique plane of the bar patterns at a 30° pitch also shows super-resolution, with visibility of frequencies up to 4.75 lp/mm. (c) At a 60° pitch, the highest frequency with detectable modulation is 3.0 lp/mm. This result illustrates that super-resolution is not achievable at pitches approaching 90°.

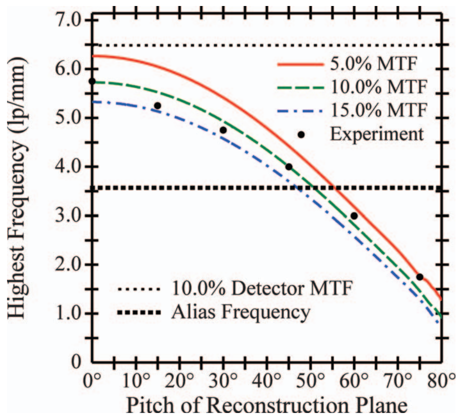


FIG. 11. Using the experimental reconstructions, the highest frequency with detectable modulation is plotted versus the pitch of the bar pattern phantom. In addition, the analogous results derived from the analytical model are shown using MTF thresholds of 5.0%, 10.0%, and 15.0%. The experimental results follow the same trend as the analytical model.

Pearson's correlation coefficient is calculated. Pearson's correlation coefficient quantifies the extent to which the experimental and analytical results are linearly dependent on a scale from −100% to 100%. One can show that there is 99.7% correlation between the six experimental points and the six corresponding analytical points. This result holds for each of the three MTF thresholds in Fig. 11. Thus, the experimental and analytical results effectively follow the same trend with pitch, regardless of the specific MTF threshold that is used in the model.

The highest frequency that can be resolved in a single projection is the alias frequency of the detector. Using Fig. 11, one can calculate the pitch at which the highest frequency with detectable modulation exactly matches the alias frequency of the detector (3.6 lp/mm). For a MTF threshold of 10.0% and a depth of 5.0 cm, this pitch is 51°. This result suggests that a 51° angle is a practical upper limit for the pitch at which a reconstruction should be generated. Figure 11 presumes that the object is relatively thin (0.05 mm thick). Because a clinical reconstruction consists of objects with various thicknesses, future work is necessary to determine the range of pitches at which clinical reconstructions are appropriate.

## 5. CLINICAL RESULTS

In breast imaging, super-resolution has application in the visualization of fine structural details, such as microcalcifications. This concept is illustrated in Fig. 12 which builds upon

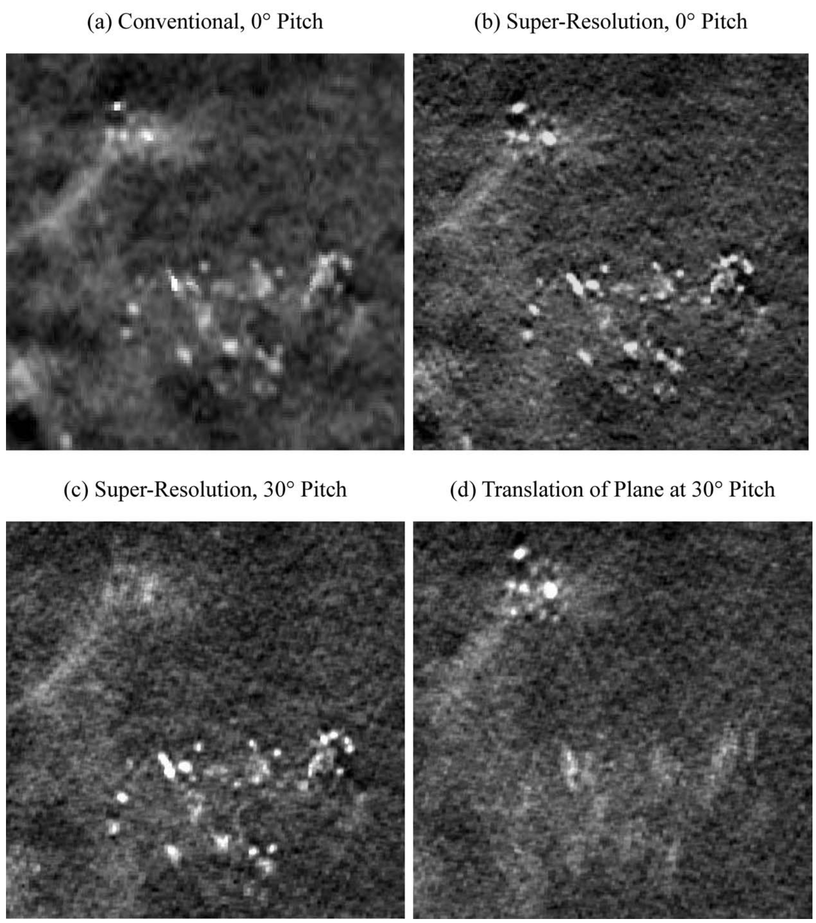


FIG. 12. In breast imaging, the concepts studied in this work have applications in the visualization of microcalcifications. (a) A slice at a 0° pitch in a BPF reconstruction is initially created using pixels matching the detector element size (140 $\mu$m), and the result is magnified to give the image displayed. (b) A slice at a 0° pitch is generated using a reconstruction grid with much smaller pixelation than the detector. (c) Using the same reconstruction grid size as image (b), the pitch of the reconstruction plane is changed to 30°. (d) The oblique reconstruction plane in image (c) is orthogonally translated by 5.0 mm to bring the upper left cluster of calcifications into focus. Images (b)–(d) support super-resolution, unlike image (a).

a clinical case presented in our earlier work. This figure differs slightly from our earlier work (Fig. 12 in Acciavatti and Maidment[5]) in terms of the region of interest (ROI) size and the reconstruction parameters. Figure 12(a) is created by magnifying a slice at a 0° pitch using 140 $\mu$m voxels matching the detector element size. The net result has 35 $\mu$m voxels. By contrast, Fig. 12(b) is a reconstruction of the same clinical case using much smaller pixelation than the detector, yielding a sharper image that supports super-resolution. In Fig. 12(c), a slice is generated at a 30° pitch using the same pixelation as Fig. 12(b). Figure 12(c) demonstrates that the visibility of the lower cluster of calcifications is not considerably different from Fig. 12(b). The impact of super-resolution is evident in the oblique reconstruction plane.

The upper left cluster of calcifications is not visible at the 30° pitch in Fig. 12(c), as it is out of the reconstruction plane. Visualization is improved by orthogonally translating the reconstruction plane by 5.0 mm [Fig. 12(d)]. The calcifications are sharper in Fig. 12(d) than in Fig. 12(a), reflecting the effect of super-resolution.

It appears that a greater number of calcifications in the upper left cluster are visible in Fig. 12(d) than in Fig. 12(b). It also appears that some of the individual calcifications can be seen with higher contrast in Fig. 12(d) than in Fig. 12(b). This result might suggest that the upper left cluster is obliquely pitched relative to the breast support and is best visualized in an oblique reconstruction plane (Fig. 13). While it would be reasonable to assume that a reconstruction is optimally viewed along the actual pitch of the calcification cluster, it is not possible to determine this optimal pitch due to the lack of ground truth in clinical images. In addition, it is not possible to determine whether the increase in contrast for some of the individual calcifications in Fig. 12(d) is due to random effects. The development of a framework for determining the optimal pitch for viewing a clinical reconstruction is beyond the scope of this work, but should be the subject of future phantom simulation studies in which ground truth is known. Future work

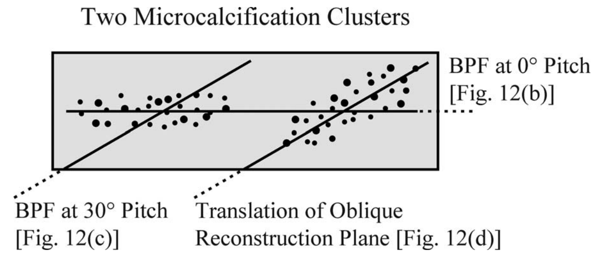


FIG. 13. A sketch of microcalcification clusters at two orientations is shown. It is posited that the calcification cluster in Fig. 12(d) is obliquely pitched relative to the breast support, unlike the cluster in Fig. 12(c).

should also investigate techniques for optimizing the filter in oblique reconstructions.

Oblique reconstructions also have application in quantifying the size of a complex cancer. Figure 14 shows the reconstruction of a clinical example using slices at 0° and 38° angles relative to the breast support. It appears that the full extent of the lesion can be seen more clearly in the oblique plane than in the plane parallel to the breast support. It also appears that the tumor margins are defined more precisely in the oblique plane. A future clinical study is merited to quantify the clinical impact of oblique reconstructions in tomosynthesis.

## 6. DISCUSSION

Our preceding paper[7] gave a proof-of-principle justification for oblique reconstructions in tomosynthesis. Because simplifying assumptions about the acquisition geometry were made in that paper, it was not explicitly demonstrated that oblique reconstructions are capable of super-resolution. By modeling detector pixelation and additional features of the acquisition geometry, this current study shows that input frequencies exceeding the detector alias frequency are indeed resolvable in an oblique reconstruction. The features of the

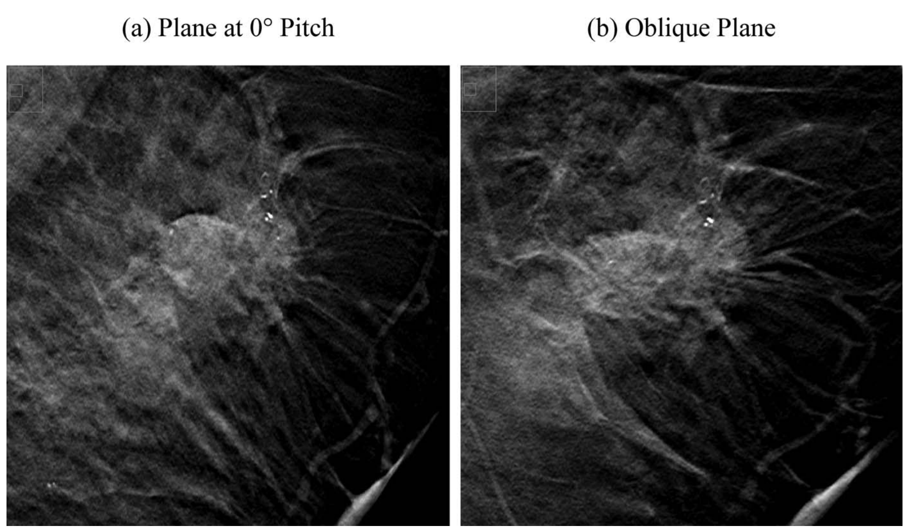


FIG. 14. (a) A reconstruction plane at a 0° angle relative to the breast support does not show the full extent of a complex cancer in this anecdotal example. (b) A plane at a 38° angle relative to the breast support appears to show the full extent of the lesion more clearly and to define the borders of the tumor more precisely.

TABLE I. In simulating the reconstruction of a pitched sine plate (Fig. 1), this work models features of the tomosynthesis acquisition geometry that were not modeled in our preceding paper (Ref. 7). The most important feature for demonstrating the existence of super-resolution is detector pixelation.

| Preceding paper (Part I) (Ref. 7) | Current paper (Part II) |
|---|---|
| Non-pixelated detector | Pixelated detector |
| Stationary detector | Rotating detector |
| 2D reconstruction space | 3D reconstruction space |
| Parallel x-ray beam geometry | Divergent x-ray beam geometry |
| Infinitesimally small angular spacing between projections | Discrete step angles between projections |

acquisition geometry that are modeled in this work, but not in our preceding paper,[7] are summarized in Table I.

In order for a test frequency to be visualized in an image, it is necessary for the MTF to exceed the detectability limit (10.0%). This work demonstrates that an object must be thin for frequencies exceeding the detector alias frequency to have detectable MTF in an oblique reconstruction. This constraint does not hold for low frequency objects, which are detectable in oblique reconstructions at larger thicknesses.

The $r$-factor was investigated as a metric for assessing the depth dependency of super-resolution. In oblique reconstruction planes centered about the mid PA/SS plane, it was demonstrated that the depth dependency of the $r$-factor is minimized with increasing pitch. Thus, one benefit of increasing the pitch of the reconstruction plane is minimizing the anisotropies in super-resolution.

The existence of super-resolution in oblique reconstructions was validated with a commercial DBT system by analyzing a bar pattern phantom. Super-resolution is achievable up to a 51° pitch in the Selenia Dimensions geometry, assuming that the input object is thin. As we noted in our earlier work,[5] the feasibility of super-resolution is not necessarily unique to the commercial DBT system analyzed or to the commercial reconstruction algorithm used. A necessary constraint is that the reconstruction algorithm supports finer sampling than the detector. The range of pitches at which super-resolution is achievable is dependent upon the design of the acquisition geometry.

By using modulation as the metric of detectability, this work implicitly assumes that noise does not influence the visibility of an object. This assumption is valid for a high contrast bar pattern phantom, as was the case in the experimental images. If one were to consider low contrast signals, the relative signal-to-noise would be a more useful metric of detectability. Future work should expand the analytical model to simulate quantum noise at various radiation dose levels, as well as other noise sources.[13,14] The highest detectable frequency in an oblique reconstruction plane [Figs. 6(c) and 11] could then be calculated as a function of the radiation dose.

Although the 2D MTF for a slice in the reconstruction is used as a metric of image quality in this work (Fig. 5), our previous study demonstrated that 3D MTF can also be used as a metric of image quality.[7] In that study, we showed that the 3D MTF is nonzero within a region resembling a double cone in the $f_x$-$f_z$ planes of Fourier space (see Fig. 1 of Acciavatti and Maidment[7]). The opening angle of the sampling cones matches the angular range of the scan. Since the 0° pitch is contained within the sampling cones in a parallel-beam geometry, conventional practice is to create slices along this pitch. It is important to note that the 0° pitch is not necessarily contained within the sampling cones in a divergent-beam geometry. At the corner of the detector opposite the chest wall, for example, the incident angle ($\theta_n$) varies over 15 projections between 22.9° and 26.3° in the Selenia Dimensions system with a 24.0 × 29.0 cm detector FOV. In this example, an important distinction must be drawn between the 3D MTF and the inplane MTF. Although the 3D MTF is zero along the 0° pitch of Fourier space, the 2D MTF of a slice along this pitch is nonzero. This property arises because the in-plane MTF is the integral of the 3D MTF along the direction perpendicular to the slice.

In order to view a reconstruction using an oblique plane, this work assumes that the conventional reconstruction planes perpendicular to the $z$ axis are rotated about the $y$ axis, or the chest wall-to-nipple direction in a breast application. Oblique reconstruction planes can also be generated by a rotation about the $x$ axis, or the direction parallel to the chest wall side of the breast support. Using the conventional definition of Euler angles, the latter rotation is termed a "roll" instead of a "pitch." Roll rotations were not modeled in this study, although we have successfully investigated these experimentally (images not shown). Roll rotations should be investigated in future work to generalize the calculation of the highest detectable frequency [Figs. 6(c) and 11] to various pitch and roll combinations.

This paper simulates a point-like focal spot with a MTF of unity at all frequencies. Future work should model the MTF due to the finite size of the focal spot. Since the MTF of the focal spot decreases with increasing magnification,[12,15–17] it is expected that resolution should become poorer with increasing depth ($z_0$) in the reconstruction. Although this effect was not modeled in this paper, the loss of resolution is evident if one compares the bar pattern reconstruction at a 0° pitch [Fig. 10(a)] against our previous work on super-resolution.[5] Using the same experimental system and acquisition parameters, our previous work demonstrated that frequencies up to 6.0 lp/mm have detectable modulation, yet our current work shows frequencies up to 5.75 lp/mm (Fig. 11). Because our current experimental results correspond to a higher depth ($z_0 = 10.8$ cm) than our previous experimental results ($z_0 = 5.0$ cm), poorer resolution is expected due to the increased focal spot magnification.

A few additional directions for more complete modeling in future work are now noted. Future work should simulate blurring in the x-ray converter, so that total attenuation in Eq. (27) is convolved with a point spread function (PSF). Blurring in the x-ray converter is most pronounced at the edges and corners of the detector due to increasing deviation in the angle of x-ray incidence relative to the normal to the detector. Previous studies have calculated the MTF degradation due to oblique x-ray incidence.[18–25]

Detector lag and ghosting are additional concepts that would be useful to model in future studies.[26–28] Although this work implicitly assumes the presence of a monoenergetic x-ray beam, polyenergetic x-ray spectra[29–31] should also be simulated in future work. Finally, the MTF degradation due to continuous x-ray tube motion during the scan of the projections should be simulated.[2,6,10,32–34] While these subtleties of the acquisition geometry were not modeled directly in this paper, the simulations showed reasonably good agreement with the experimental results for the purpose of this work.

## 7. CONCLUSION

This work demonstrates the existence of super-resolution in oblique reconstructions for tomosynthesis. We show that test frequencies exceeding the detector alias frequency can be resolved in an oblique plane created with pixelation smaller than the detector element size. The test object must be thin in order for high frequencies to have detectable modulation.

Experimental images of a thin bar pattern phantom verified the existence of super-resolution in oblique reconstructions. In accord with the predictions of the analytical model, the range of frequencies with detectable modulation decreased with increasing pitch, so that only low frequency objects could be detected at pitches approaching 90°. This limiting case corresponds to a test frequency perpendicular to the breast support in the DBT system used for experimental validation. In breast imaging, super-resolution has application in the visualization of microcalcifications and other subtle signs of cancer.

## ACKNOWLEDGMENTS

The authors thank Roshan Karunamuni for helping to assemble the goniometry stand for experimental images. In addition, the authors acknowledge Stewart Mein for his assistance with the acquisition and reconstruction of early bar pattern images. Finally, the authors thank Johnny Kuo, Susan Ng, and Peter Ringer (Real Time Tomography, LLC, Villanova, PA) for providing helpful guidance in the use of the reconstruction software for experimental images. Andrew D. A. Maidment is a member of the Scientific Advisory Board of Real Time Tomography. The project described was supported by predoctoral training Grant No. W81XWH-11-1-0100 through the Department of Defense Breast Cancer Research Program. The content is solely the responsibility of the authors and does not necessarily represent the official views of the funding agency. Support for Real Time Tomography was provided separately in part through NIH Grant No. R43EB007140/R44EB007140.

## APPENDIX: NOMENCLATURE

| Symbol | Meaning |
|---|---|
| $\mathcal{A}\mu(n)$ | Total attenuation for the $n$th projection |
| $\mathcal{D}\mu(\mathbf{m}, n)$ | Signal in the **m**th detector element for the $n$th projection |
| $\mathcal{F}$ | Fourier transform operator (subscript denotes dimension) |
| $\mathcal{L}_n$ | Path length through the input for the $n$th projection |
| $\mathbb{R}^3$ | Euclidean 3-space |
| $\mathcal{S}\mu$ | Raw signal at coordinate $(u_1, u_2)$ on the rotated detector |
| $\alpha_y$ | Pitch angle, corresponding to a rotation about the $y$ axis |
| $\gamma_n$ | Angle of rotation of the detector relative to the $x$ axis for the $n$th projection |
| $\Delta\psi$ | Angular spacing between projections |
| $\varepsilon$ | Thickness of sine plate (Fig. 1) |
| $\eta''_{x\mathbf{m}n}$ | A term defined by Eq. (45) to simplify intermediate calculations |
| $\eta''_{y\mathbf{m}n}$ | A term defined by Eq. (36) to simplify intermediate calculations |
| $\theta_n$ | Angle of x-ray incidence relative to the normal to the detector ($\theta_{\mathbf{m}n}$ denotes the special case at the centroid of the **m**th detector element for the $n$th projection) |
| $\kappa_n$ | A quantity defined by Eq. (23) |
| $\lambda_n$ | A quantity defined by Eq. (24) |
| $\mu$ | X-ray linear attenuation coefficient of input object (sine plate) |
| $\xi$ | Truncation frequency of reconstruction filter |
| $\rho_1,\rho_2$ | Quantities defined in our previous work.[5] |
| $\sigma_{j\mathbf{m}n}$ | Terms defined in our previous work.[5] |
| $\phi$ | Reconstruction filter |
| $\psi_n$ | Nominal projection angle |
| $a_x,a_y$ | Detector element dimensions in the $x$ and $y$ directions; if the $x$ and $y$ subscripts are removed, the detector element is square ($a_x = a_y = a$) |
| $b_1,b_2$ | Real numbers used to illustrate a sum-to-product trigonometric identity [Eq. (25)] |
| $C$ | Maximum value of the attenuation coefficient of the sine plate [Eq. (4)] |
| COR | Center-of-rotation of x-ray tube motion |
| CT | Computed tomography |
| DBT | Digital breast tomosynthesis |
| DM | Digital mammography |
| $f$ | Spatial frequency ($f_0$ denotes the input frequency) |
| FBP | Filtered backprojection |
| FOV | Field-of-view |
| $g$ | Gear ratio of detector |
| $h$ | Source-to-COR distance for rotating x-ray tube |
| $i$ | Imaginary unit given as $\sqrt{-1}$ |
| $I''_{x\mathbf{m}n}$ | An integral defined by Eq. (41) |
| $I''_{y\mathbf{m}n}$ | An integral defined by Eq. (35) |
| $l$ | Distance between the COR and the origin O (Fig. 1) |
| lp | Line pairs |
| $\mathbf{m}$ | A doublet with coordinates $(m_x, m_y)$ used for labeling detector elements |
| $M$ | Magnification |
| MTF | Modulation transfer function |
| $n$ | Projection number |

| | |
|---|---|
| $N$ | Total number of projections |
| PA | Posteroanterior (in breast x-ray imaging, the direction perpendicular to the chest wall) |
| PA/SS | Descriptive acronym for a plane with extent along the PA and SS directions |
| PSF | Point spread function |
| $r$ | Ratio of the amplitude at the highest Fourier peak less than the detector alias frequency ($0.5a^{-1}$) to the amplitude at the input frequency (e.g., 5.0 lp/mm) in reconstructing a high frequency sine plate (Fig. 1) |
| RA | Ramp filter |
| ROI | Region of interest |
| SA | Spectrum apodization filter |
| SBP | Simple backprojection |
| SS | Source-to-support (defined to be synonymous with the $z$ direction) |
| $T$ | Period of input waveform (Fig. 3) |
| TFT | Thin-film transistor |
| $u_1$,$u_2$ | Position in the plane of the rotated detector (parallel and perpendicular to the chest wall, respectively) |
| $w$ | Parameter ranging between 0 and 1 in the equation of the x-ray beam between the focal spot and the incident point on the detector [Eq. (16)] |
| $w_n^{\pm}$ | Value of $w$ at the entrance ($w_n^+$) and exit ($w_n^-$) points of the x-ray beam through the sine plate (Fig. 1) for the $n$th projection |
| $x$ | Position parallel to the chest wall side of the breast support; rotation by the angle $\gamma_n$ about the $y$ axis yields $x'_n$ |
| $x''$ | Position along the pitch angle $\alpha_y$ of an oblique reconstruction plane relative to the point $(x_0, y_0, z_0)$ in Eq. (30) |
| $(x_0, y_0, z_0)$ | Centroid of an oblique reconstruction plane [Eq. (30)] |
| $x_n^{\pm}$ | Value of $x$ at the entrance ($x_n^+$) and exit ($x_n^-$) points of the x-ray beam through the sine plate (Fig. 1) for the $n$th projection |
| $y$ | Position perpendicular to the chest wall; it is equivalent to $y'_n$ |
| $y''$ | Position perpendicular to the plane of x-ray tube motion relative to the point $(x_0, y_0, z_0)$ in Eq. (30) |
| $z$ | Position perpendicular to the plane of the breast support; rotation by the angle $\gamma_n$ about the $y$ axis yields $z'_n$ |
| $z''$ | Position perpendicular to an oblique reconstruction plane relative to the point $(x_0, y_0, z_0)$ in Eq. (30) |

[a]Author to whom correspondence should be addressed. Electronic mail: Andrew.Maidment@uphs.upenn.edu; Telephone: +1-215-746-8763; Fax: +1-215-746-8764.

[1]R. J. Acciavatti and A. D. A. Maidment, "Investigating the potential for super-resolution in digital breast tomosynthesis," in *SPIE Medical Imaging*, edited by N. J. Pelc, E. Samei, and R. M. Nishikawa (SPIE, Lake Buena Vista, FL, 2011), pp. 1–12.

[2]R. J. Acciavatti and A. D. A. Maidment, "Optimization of continuous tube motion and step-and-shoot motion in digital breast tomosynthesis systems with patient motion," in *SPIE Medical Imaging*, edited by N. J. Pelc, R. M. Nishikawa, and B. R. Whiting (SPIE, San Diego, CA, 2012), pp. 1–12.

[3]R. J. Acciavatti and A. D. A. Maidment, "Proposing an acquisition geometry that optimizes super-resolution in digital breast tomosynthesis," Lect. Notes Comput. Sci. **7361**, 386–393 (2012).

[4]R. J. Acciavatti, S. B. Mein, and A. D. A. Maidment, "Investigating oblique reconstructions with super-resolution in digital breast tomosynthesis," Lect. Notes Comput. Sci. **7361**, 737–744 (2012).

[5]R. J. Acciavatti and A. D. A. Maidment, "Observation of super-resolution in digital breast tomosynthesis," Med. Phys. **39**(12), 7518–7539 (2012).

[6]R. J. Acciavatti, P. R. Bakic, and A. D. A. Maidment, "Proposing a new velocity profile for continuous X-ray tube motion in digital breast tomosynthesis," in *SPIE Medical Imaging*, edited by R. M. Nishikawa, B. R. Whiting, and C. Hoeschen (SPIE, Lake Buena Vista, FL, 2013), pp. 1–10.

[7]R. J. Acciavatti and A. D. A. Maidment, "Oblique reconstructions in tomosynthesis. I. Linear systems theory," Med. Phys. **40**, 111911 (21pp.) (2013).

[8]M. Lanyi, "Differential diagnosis of microcalcifications," *Diagnosis and Differential Diagnosis of Breast Calcifications* (Springer-Verlag, Berlin, 1988), Chap. 7, pp. 193–231.

[9]J. Kuo, P. A. Ringer, S. G. Fallows, P. R. Bakic, A. D. A. Maidment, and S. Ng, "Dynamic reconstruction and rendering of 3D tomosynthesis images," in *SPIE Medical Imaging*, edited by N. J. Pelc, E. Samei, and R. M. Nishikawa (SPIE, Lake Buena Vista, FL, 2011), pp. 1–11.

[10]B. Zhao and W. Zhao, "Three-dimensional linear system analysis for breast tomosynthesis," Med. Phys. **35**(12), 5219–5232 (2008).

[11]D. L. Lee, L. K. Cheung, B. Rodricks, and G. F. Powell, "Improved imaging performance of a 14 × 17-inch Direct Radiography (TM) System using Se/TFT detector," in *SPIE Conference on Physics of Medical Imaging*, edited by T. James, I. Dobbins, and J. M. Boone (SPIE, San Diego, CA, 1998), pp. 14–23.

[12]H. E. Johns and J. R. Cunningham, "Diagnostic radiology," *The Physics of Radiology*, 4th ed. (Thomas, Springfield, IL, 1983), Chap. 16, pp. 557–669.

[13]H. H. Barrett and K. J. Myers, "Poisson statistics and photon counting," in *Foundations of Image Science*, edited by B. E. A. Saleh (Wiley, New York, NY, 2004), Chap. 11, pp. 631–699.

[14]H. H. Barrett and K. J. Myers, "Noise in detectors," in *Foundations of Image Science*, edited by B. E. A. Saleh (Wiley, New York, NY, 2004), Chap. 12, pp. 701–800.

[15]J. T. Bushberg, J. A. Seibert, E. M. Leidholdt, Jr., and J. M. Boone, "Mammography," *The Essential Physics of Medical Imaging*, 2nd ed. (Lippincott, Philadelphia, PA, 2002), Chap. 8, pp. 191–229.

[16]J. T. Bushberg, J. A. Seibert, E. M. Leidholdt, Jr., and J. M. Boone, "Image quality," *The Essential Physics of Medical Imaging*, 2nd ed. (Lippincott, Philadelphia, PA, 2002), Chap. 10, pp. 255–291.

[17]J. T. Bushberg, J. A. Seibert, E. M. Leidholdt, Jr., and J. M. Boone, "Computed tomography," *The Essential Physics of Medical Imaging*, 2nd ed. (Lippincott, Philadelphia, PA, 2002), Chap. 13, pp. 327–372.

[18]W. Que and J. A. Rowlands, "X-ray imaging using amorphous selenium: Inherent spatial resolution," Med. Phys. **22**(4), 365–374 (1995).

[19]G. Hajdok and I. A. Cunningham, "Penalty on the detective quantum efficiency from off-axis incident x rays," in *Medical Imaging 2004: Physics of Medical Imaging*, edited by M. J. Yaffe and M. J. Flynn (SPIE, San Diego, CA, 2004), pp. 109–118.

[20]J. G. Mainprize, A. K. Bloomquist, M. P. Kempston, and M. J. Yaffe, "Resolution at oblique incidence angles of a flat panel imager for breast tomosynthesis," Med. Phys. **33**(9), 3159–3164 (2006).

[21]R. J. Acciavatti and A. D. A. Maidment, "Calculation of OTF, NPS, and DQE for oblique x-ray incidence on turbid granular phosphors," Lect. Notes Comput. Sci. **6136**, 436–443 (2010).

[22]M. Freed, S. Park, and A. Badano, "A fast, angle-dependent, analytical model of CsI detector response for optimization of 3D x-ray breast imaging systems," Med. Phys. **37**(6), 2593–2605 (2010).

[23]M. Freed, S. Park, and A. Badano, "Erratum: "A fast, angle-dependent, analytical model of CsI detector response for optimization of 3D x-ray breast imaging systems" [Med. Phys. **37**, 2593–2605 (2010)]," Med. Phys. **38**(4), 2307 (2011).

[24]A. Badano, M. Freed, and Y. Fang, "Oblique incidence effects in direct x-ray detectors: A first-order approximation using a physics-based analytical model," Med. Phys. **38**(4), 2095–2098 (2011).

[25] R. J. Acciavatti and A. D. A. Maidment, "Optimization of phosphor-based detector design for oblique x-ray incidence in digital breast tomosynthesis," Med. Phys. **38**(11), 6188–6202 (2011).
[26] A. K. Bloomquist, M. J. Yaffe, G. E. Mawdsley, and D. M. Hunter, "Lag and ghosting in a clinical flat-panel selenium digital mammography system," Med. Phys. **33**(8), 2998–3005 (2006).
[27] J. H. Siewerdsen and D. A. Jaffray, "A ghost story: Spatio-temporal response characteristics of an indirect-detection flat-panel imager," Med. Phys. **26**(8), 1624–1641 (1999).
[28] W. Zhao, G. DeCrescenzo, S. O. Kasap, and J. A. Rowlands, "Ghosting caused by bulk charge trapping in direct conversion flat-panel detectors using amorphous selenium," Med. Phys. **32**(2), 488–500 (2005).
[29] D. M. Tucker, G. T. Barnes, and D. P. Chakraborty, "Semiempirical model for generating tungsten target x-ray spectra," Med. Phys. **18**(2), 211–218 (1991).
[30] J. M. Boone, T. R. Fewell, and R. J. Jennings, "Molybdenum, rhodium, and tungsten anode spectral models using interpolating polynomials with application to mammography," Med. Phys. **24**(12), 1863–1874 (1997).
[31] M. M. Blough, R. G. Waggener, W. H. Payne, and J. A. Terry, "Calculated mammographic spectra confirmed with attenuation curves for molybdenum, rhodium, and tungsten targets," Med. Phys. **25**(9), 1605–1612 (1998).
[32] B. Ren, C. Ruth, J. Stein, A. Smith, I. Shaw, and Z. Jing, "Design and performance of the prototype full field breast tomosynthesis system with selenium based flat panel detector," in *SPIE*, edited by M. J. Flynn (SPIE, San Diego, CA, 2005), pp. 550–561.
[33] E. Shaheen, N. Marshall, and H. Bosmans, "Investigation of the effect of tube motion in breast tomosynthesis: Continuous or step and shoot?" in *SPIE Medical Imaging*, edited by N. J. Pelc, E. Samei, and R. M. Nishikawa (SPIE, Lake Buena Vista, FL, 2011), pp. 1–9.
[34] R. Peng *et al.*, "An experimental comparison of continuous motion and step-and-shoot modes in digital breast tomosynthesis," Lect. Notes Comput. Sci. **7361**, 650–657 (2012).